International Journal of Numerical Methods for Heat & Fluid Flow

ISSN: 0961-5539; Impact Factor: 2.450; Publisher: Emerald Publishing.

(Accepted July 28th 2020)

COMPUTATION OF NON-SIMILAR FLOW OF A MAGNETIC PSEUDOPLASTIC NANOFLUID OVER A CIRCULAR CYLINDER WITH VARIABLE THERMOPHYSICAL PROPERTIES AND RADIATIVE FLUX

H. Thameem Basha[1*], R. Sivaraj[1], V. Ramachandra Prasad[1] *and* O. Anwar Beg[2]

[1]*Dept. Mathematics, School of Advanced Sciences, Vellore Institute of Technology, Vellore 632014, India*

[2] *Professor of Engineering Science, Aeronautical and Mechanical Engineering Department, School of Science, Engineering and Environment (SEE), University of Salford, Manchester M54WT, UK*

Corresponding author- Email address: basha.thameem66@gmail.com (H. Thameem Basha1)

ABSTRACT

Generally, in computational thermofluid dynamics, the thermophysical properties of fluids (e.g. viscosity and thermal conductivity) are considered as constant. However, in many applications, the variability of these properties plays a significant role in modifying transport characteristics while the temperature difference in the boundary layer is notable. These include drag reduction in heavy oil transport systems, petroleum purification and coating manufacturing. Motivated by the last of these applications, in the current study, a comprehensive mathematical model is developed to explore the impact of variable viscosity and variable thermal conductivity characteristics in magnetohydrodynamic non-Newtonian nanofluid enrobing boundary layer flow over a horizontal circular cylinder in the presence of cross diffusion (Soret and Dufour effects) and appreciable thermal radiative heat transfer under a static radial magnetic field. The Williamson pseudoplastic model is deployed for rheology of the nanofluid. Buongiornos two component model is employed for nanoscale effects. The dimensionless nonlinear partial differential equations have been solved by using an implicit finite difference Keller box scheme. Extensive validation with earlier studies in the absence of nanoscale and variable property effects is included. The influence of notable parameters like Weissenberg number, variable viscosity, variable thermal conductivity, Soret and Dufour numbers on heat, mass and momentum characteristics are scrutinized and visualized via graphs and tables. The outcomes disclose that the Williamson nanofluid velocity declines by enhancing the Lorentz hydromagnetic force in the radial direction. Thermal and nanoparticle concentration boundary layer thickness are enhanced with greater streamwise coordinate values. An increase in Dufour number or a decrease in Soret number slightly enhances the nanofluid temperature and thickens the thermal boundary layer. Flow deceleration is induced with greater viscosity parameter. Nanofluid temperature is elevated with greater Weissenberg number and thermophoresis nanoscale parameter.

Keywords: Magnetohydrodynamics; Buongiorno nanofluid model; Williamson rheological model; Variable viscosity; Variable thermal conductivity.

Nomenclature

a	radius of the cylinder $[m]$
B_0	strength of the constant magnetic field $[kg\ s^{-2}\ A^{-1}]$
C	concentration of the fluid $[kg\, m^{-3}]$
C_f^*	skin friction coefficient
$(C_p)_f$	specific heat of fluid $[J\ kg^{-1}K^{-1}]$
C_S	concentration susceptibility
C_W	concentration at the surface $[kg\, m^{-3}]$
C_∞	ambient concentration $[kg\, m^{-3}]$
D_B	Brownian diffusion $[m^2\ s^{-1}]$
D_u	Dufour number
D_T	thermophoretic diffusion $[m^2\ s^{-1}]$
g_a	acceleration due to gravity $[m\ s^{-2}]$
Gr	Grashof number
k	constant fluid thermal conductivity $[W\ m^{-1}\ K^{-1}]$
k_a	mean absorption coefficient $[m^{-1}]$
k_f	fluid thermal conductivity $[W\ m^{-1}\ K^{-1}]$
K_T	thermal diffusion $[m^2\ s^{-1}]$
M_a	magnetohydrodynamic parameter
N_B	Brownian motion parameter
N_r	species to thermal buoyancy ratio parameter
N_T	thermophoresis parameters
Nu^*	Nusselt number
Pr	Prandtl number
R_a	Rosseland conduction-radiation parameter
Sc	Schmidt number
Sh^*	Sherwood number
S_r	Soret number
T	temperature of the fluid $[K]$
T_m	mean fluid temperature $[K]$
T_W	temperature at the surface $[K]$
T_∞	ambient temperature $[K]$
u, v	velocity components in x, y directions $[\mathrm{m\,s^{-1}}]$
We	Weissenberg number
x, y	Cartesian coordinates $[m]$

Greek symbols

β_1	coefficient of nonlinear thermal expansion $[K^{-1}]$
Γ	material constant
γ^*	variable viscosity parameter
δ^*	variable thermal conductivity parameter
μ	constant dynamic viscosity $[kg\ m^{-1}\ s^{-1}]$
μ_f	dynamic viscosity $[kg\ m^{-1}\ s^{-1}]$
ρ_f	density of fluid $[kg\ m^{-3}]$
ρ_p	density of particle $[kg\ m^{-3}]$
ν_f	kinematic viscosity $[m^2\ s^{-1}]$
σ	electrical conductivity $[S\ m^{-1}]$
σ_B	Stefan Boltzmann constant $[= 1.3807 \times 10^{-23} J\ K^{-1}]$
τ	ratio between particle and base fluid
τ^*	shear stress sensor

1. Introduction

Molecular transport in a binary mixture driven by a temperature gradient is known as the thermo-diffusion (Soret) effect while molecular transport caused by a concentration gradient is known as the diffusion-thermo (Dufour) effect. Collectively, these cross-diffusion effects are often neglected because of the order of magnitude is smaller than effects expressed by means of Fourier and Fick laws. The Soret effect is quite important when higher density differences exist in fluid transport. The Dufour effect is ineffective in a mixture of various liquids although it can exert a notable impact in gases diffusing in liquids. Soret and Dufour effects also play a major role in a mixture of gases between very light (Hydrogen, Helium) and medium (Nitrogen, air) molecular weights as deployed in isotope separation. Heat transfer properties are strongly coupled with mass transfer properties when double-diffusive (thermo-solutal) convection is considered with the influence of Soret and Dufour numbers. Soret and Dufour effects also feature extensively in various engineering technologies and industrial processes including the solidification of binary alloys, crystal growth, contaminant transport in groundwater, pollutant movement, chemical reactors, magmatic geophysical flows, oceanography, underground treatment of nuclear waste materials and drying technologies [Beg et al. (2009a); Beg et al. (2009b); Kumar and Sivaraj(2013); Rashad and Chamkha (2014); Raju and Sandeep (2016); Reddy and Chamkha(2016); Ruhail et al.(2017); Muthtamilselvan et al. (2018)]. Sivaraj et al. (2019) examined the cross-diffusion (Soret and Dufour) effects on Casson fluid flow with variable fluid properties and observed that higher values of Dufour effect or lower values of the Soret effect elevate Casson fluid temperature. Makinde and Olanrewaju (2011a) discussed the time-dependent mixed convective flow over a moving permeable plate with the influence of Soret and Dufour effects and found that the velocity of the fluid decreases with an increase in the Soret effect. Pal et al. (2016) used a numerical method to explore the Soret and Dufour impacts on three different water-based nanofluids over a plate and deduced that the water nanofluid concentration decays as a result of increasing Soret number or with decreasing Dufour number. Other studies include Beg et al. (2011) on micropolar coating flows, Beg et al. (2019) on MHD ocean generators and very recently Bhatti et al. (2020) on ferro-magnetic transport properties.

The vast majority of analytical boundary layer flow studies have been confined to constant thermo-physical properties of the fluid. When there is a high-temperature difference between the surface and the fluid in the boundary layer, the thermo-physical properties of the fluid can vary notably. Compared with other thermo-physical properties, the fluid viscosity is highly sensitive to temperature. For instance, in lubricating liquids, heat is produced as a result of internal friction which causes a change in the viscosity of the fluid. The absolute viscosity of water declines by 240% due to an increase in temperature from 100^o C to 500^o C. As a result, it is logical to consider variable viscosity in order to more precisely determine transport characteristics. Varying viscosity with respect to temperature arises in many branches of modern technology including smart coating enrobing, drawing of plastic films, surfacial spray deposition, glass fiber production, petroleum refinement, fabrication of thin film concentrating solar receivers, food processing, gas turbine film cooling, fluid film tribology etc [Manjunatha and Gireesha(2016); Sheikholeslami and Rokni (2017); Astanina et al.(2019); Makinde and Chinyoka(2012); Salahuddin et al.(2019); Kumar and Sivaraj (2013)]. Animasaun (2015) reported a numerical study of free convective flow of Casson fluid over a plate with the cross-diffusion, showing that higher viscosity parameter reduces the Casson fluid temperature. Reddy et al. (2018) utilized a Crank Nicholson scheme to explore fluid transport property influence on entropy generation in time-dependent viscoelastic (Reiner Rivlin second grade) polymeric fluid flow and observed that a boost in viscosity parameter enhances entropy heat generation. Mehmood et al. (2018) exhibited the influence of variable viscosity on non-orthogonal stagnation flow of Cu-water nanofluid solar gel coatings and found that increasing nanoparticle volume fraction decelerates flow. Hayat et al. (2016) analytically investigated the flow of mixed convective time-dependent over an exponential surface in the presence of temperature-dependent viscosity.

Non-Newtonian fluids are fluids which have viscosity shear-dependence in addition to shear-thinning/shear-thickening characteristics. These fluids have numerous industrial applications, including petroleum production, bionic hydrogels in robotics, chemical process industries, plastic polymers, ferrofluid lubricants, packaging materials for food preservation, cosmetic products, and manufacture of optical fibers. Non-Newtonian fluids have complex rheological characteristics, so the flow properties of such fluids cannot be elucidated by the Navier-Stokes equations which is based on the elementary Newtonian viscosity law. As a result, a diverse range of constitutive models including the Maxwell upper convected (UCM) fluid, Williamson fluid, Johnson-Segalman fluid, Cross fluid, FENE-P fluid, Walters B-fluid, PPT fluid, Casson fluid, Eringen micropolar fluid and Carreau fluid models have been proposed by various researchers. Transport characteristics of various non-Newtonian fluid models were investigated by several researchers [Gaffar et al.

(2015); Makinde et al. (2011b); Khan et al. (2019); Nadeem et al. (2017), Latiff et al. (2016), Norouzi et al. (2018) and Basha et al. (2020)]. The Williamson fluid model is a popular industrial rheological model developed originally for analyzing molten plastic molding (Williamson 1929). This fluid model expresses the exact behavior of pseudoplastic fluids which differ from ideal plastics in that there is no real yield value. Due to its shear-thinning nature, the Williamson fluid model can be used to analyze many other technological and natural liquids including blood, suspensions, magnetic polymers etc.

Nanofluids, which are suspensions of base fluids engineered to contain nanometer sized metallic or carbon-based particles (Das et al. 2007) have proved very popular in recent years due to their superior thermal conductivity properties. Recently, many researchers have theoretically and experimentally explored the heat transfer characteristics of various nanoparticles for several industrial processes, manufacturing processes, and renewable energy applications[Mansoury et al. 2019; Ma et al. 2019; Basha et al. 2019]. Nanofluids have also been shown with certain volume fractions to exhibit shear-thinning behaviour and other rheological characteristics. Several careful experimental studies have confirmed the strong non-Newtonian properties of nanofluids in a diverse array of applications ranging from thermal engineering systems (Anoop et al. 2009, Chang et al. 2019) to petroleum drilling fluids (Beg et al. (2018). Laboratory testing of nanofluid thermal enhancement features with rheological behaviour has also been accompanied with considerable numerical investigation e.g. Hussanan et al. (2017)., Kang et al. (2014). Acharya et al. (2019) addressed the multi-slip impact on Williamson nanofluid flow from a sheet, noting that the rate of heat transfer declines with increment in velocity and thermal slips. Basha et al. (2020) numerically explored the variable fluid property effects on Williamson nanofluid flow over three different geometries with wall slip mechanisms. Subbarayudu et al. (2020) used the Williamson nanofluid model to simulate blood flow over a wedge surface with radiation heat transfer, indicating that higher values of Weissenberg number (ratio of elastic to viscous forces) accentuates blood temperature.

An inspection of the literature has revealed that generally computational studies of external boundary layer flows of rheological nanofluids have featured only ordinary differential equation boundary value problems i.e. only a single space variable has been considered. Furthermore, most studies have also ignored thermophysical property variation and cross diffusion effects. The objective of the current work is therefore to present a more generalized two-dimensional approach to axisymmetric rheological nanofluid boundary layer flow from a cylindrical body with thermal radiation. The model developed also features a Williamson-Buongiorno nanofluid and includes magnetohydrodynamic, Soret and Dufour effects. Rosselands diffusion flux approximation is utilized for radiative heat transfer. These constitute the novelties

of the present work. The Williamson nanofluid viscosity and thermal conductivity are considered as variable due to temperature difference. The steady-state conservation equations are transformed, rendered non-dimensional and then solved with appropriate wall and free stream conditions by means of unconditionally stable implicit finite difference Keller box scheme. Extensive contour plots are drawn to manifest the significance of diverse multi-physical parameters on the fluid transport characteristics. Verification of the accuracy of the Keller box method with earlier published works is presented. The simulations are relevant to high-temperature magnetic nano-polymer coating flow systems (Beg et al. 2019, Dhumal et al. 2015, Hong et al. 2007, Sansom et al. 2013, Sheparovych et al. 2006, Vshivkov and Rusinova, 2017).

2. Mathematical Formulation

The schematic view of geometry for the present problem is shown in Fig. 1 in a two-dimensional Cartesian coordinate system (x, y). The viscosity and thermal conductivity variation in natural convective time independent flow of electrically conducting Williamson nanofluid (magnetic nano-polymer) over a circular cylinder is considered. A magnetic field, B_0, which is assumed to be uniform and static and is applied radially. The coordinates x and y are taken along the circumference and normal direction of the cylinder, respectively, and a is the radius of the cylinder. Changes in density for the buoyancy terms are determined by employing the Boussinesq approximation. The constant temperature (T_W) and concentration (C_W) of the wall are presumed to be greater than the ambient temperature (T_∞) and ambient concentration (C_∞), respectively. The Buongiorno (two phase) nanofluid model (Das et al. 2007) is employed to formulate the momentum, energy and nano-particle concentration equations with the following assumptions.

- Natural convection, laminar, time independent, incompressible flow of Williamson nanofluid is considered.
- The flow equation is accounting the body force.
- The induced magnetic field strength is smaller compared to the external magnetic field and hence it is neglected (small magnetic Reynolds number).
- The circular cylinder is isothermal, iso-solutal and electrically insulated.
- Soret and Dufour effects are taken into consideration.
- Hall current, ion slip and Maxwell displacement currents are neglected.

Based on the aforesaid considerations, the transport equations for the present problem in Cartesian coordinates (x, y) are [Beg et al. (2009b); Animasaun (2015); Sivaraj et al. (2019) and Acharya et al. (2019)] can be shown to take the form:

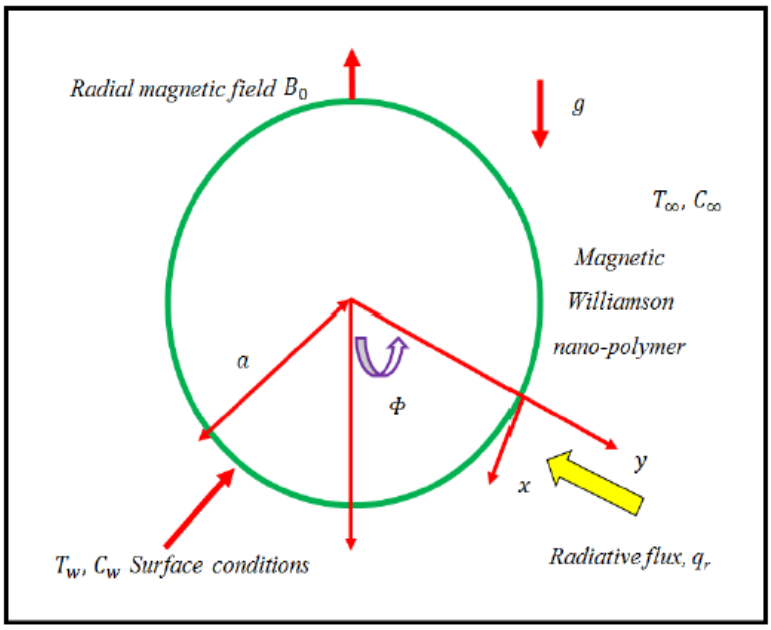

Fig. 1. Physical configuration of the problem.

$$\frac{\partial u}{\partial x}+\frac{\partial v}{\partial y}=0, \tag{1}$$

$$u\frac{\partial u}{\partial x}+v\frac{\partial u}{\partial y}=\frac{1}{\rho_f}\frac{\partial}{\partial y}\left[\mu\left(T\right)\frac{\partial u}{\partial y}\right]+\frac{\Gamma\sqrt{2}}{\rho_f}\left[\frac{\partial}{\partial y}\left\{\left[\mu\left(T\right)\frac{\partial u}{\partial y}\right]\frac{\partial u}{\partial y}\right\}\right]-\frac{\sigma B_0^2}{\rho_f}u$$
$$+g_a\left[\left(1-C_\infty\right)\rho_f\beta_1\left(T-T_\infty\right)-\left(\rho_p-\rho_f\right)\left(C-C_\infty\right)\right]\sin\left(\frac{x}{a}\right), \tag{2}$$

$$u\frac{\partial T}{\partial x}+v\frac{\partial T}{\partial y}=\frac{1}{\left(\rho C_p\right)_f}\frac{\partial}{\partial y}\left[k\left(T\right)\frac{\partial T}{\partial y}\right]+\tau\left[D_B\frac{\partial C}{\partial y}\frac{\partial T}{\partial y}+\frac{D_T}{T_\infty}\left(\frac{\partial T}{\partial y}\right)^2\right]$$
$$-\frac{1}{\left(\rho C_p\right)_f}\frac{\partial q_r}{\partial y}+D_B\frac{K_T}{\left(C_p\right)_f C_S}\frac{\partial^2 C}{\partial y^2}, \tag{3}$$

$$u\frac{\partial C}{\partial x}+v\frac{\partial C}{\partial y}=D_B\frac{\partial^2 C}{\partial y^2}+\frac{D_T}{T_\infty}\frac{\partial^2 T}{\partial y^2}+D_B\frac{K_T}{T_m}\frac{\partial^2 T}{\partial y^2}. \tag{4}$$

We further note that in the present formulation, the modified shear term in Eqn. (2) is based on the extra stress tensor for a Williamson fluid (1929) which is defined as $\chi=[\mu_\infty+(\mu_0+\mu_\infty)(1-\tau^*\Lambda)^{-1}]\mathrm{A}_1$, in which we consider $\mu_\infty=0$ and $\tau^*\Lambda<1$, with the shear stress sensor given by $\tau^*=\sqrt{\frac{\mathrm{trac}\left(\mathrm{A}_1^2\right)}{2}}$, $\mathrm{A}_1=\mathrm{grad}\mathbf{V}+[\mathrm{grad}\mathbf{V}]^T$.

The boundary conditions imposed are as follows:

$$\left.\begin{array}{l} u=0,\ v=0,\ T=T_W,\ C=C_W \quad \text{at } y=0, \\ u=0,\ T\to T_\infty,\ C\to C_\infty \qquad \text{as } y\to\infty. \end{array}\right\} \tag{5}$$

where $\nu_f = \frac{\mu_f}{\rho_f}$ and $\tau = \frac{(\rho C_p)_p}{(\rho C_p)_f}$.

Viscosity changes due to temperature can be expressed as follows[Kumar and Sivaraj(2013)]

$$\frac{\mu}{\mu_f} = 1 - \gamma\left(T - T_\infty\right), \tag{6}$$

According to Sivaraj et al. (2019), the thermal conductivity may be considered as a linear function of temperature

$$\frac{k}{k_f} = 1 + \delta\left(T - T_\infty\right), \tag{7}$$

The radiative heat flux (q_r) which is unidirectional can be written as:

$$q_r = -\frac{4}{3}\frac{\sigma_B}{k_a}\left(\frac{\partial T^4}{\partial y}\right) = -\frac{16}{3}\frac{\sigma_B T_\infty^3}{k_a}\left(\frac{\partial T}{\partial y}\right), \tag{8}$$

Let us introduce a dimensional stream function, ψ, as defined by the famous Cauchy-Riemann equations, $u = \frac{\partial(\psi(\xi,\eta))}{\partial x}$ & $v = -\frac{\partial(\psi(\xi,\eta))}{\partial y}$, in addition to suitable non-similarity variables as follows:

$$\left.\begin{array}{l} \xi = \frac{x}{a},\ \eta = (Gr)^{\frac{1}{4}}\left(\frac{y}{a}\right),\ \psi = \xi f (Gr)^{\frac{1}{4}}\nu_f, \\ T = T_\infty + \theta\left(T_W - T_\infty\right),\ C = C_\infty + \phi\left(C_W - C_\infty\right). \end{array}\right\} \tag{9}$$

By implementing the above variables, Eqns. (2)-(4) are transformed to the following non-similar form in a (ξ,η) coordinate system:

$$\begin{aligned} &\left(1-\gamma^*\theta\right) f''' + 2We\xi\left(1-\gamma^*\theta\right) f''' f'' - We\xi\gamma^*\left(f''\right)^2\theta' - \gamma^* f''\theta \\ &-\left(f'\right)^2 + ff'' + \frac{sin\,\xi}{\xi}\left(\theta - N_r\phi\right) - M_a f' = \xi\left[f'\frac{\partial f'}{\partial\xi} - f''\frac{\partial f}{\partial\xi}\right], \end{aligned} \tag{10}$$

$$\begin{aligned} &\frac{1}{\mathrm{Pr}}\left[\left(1+\delta^*\theta\right) + \frac{4}{3R_a}\right]\theta'' + \frac{\delta^*\left(\theta'\right)^2}{\mathrm{Pr}} + f\theta' + N_B\theta'\phi' \\ &\qquad + N_T\left(\theta'\right)^2 + D_u\,\phi'' = \xi\left[f'\frac{\partial\theta}{\partial\xi} - \theta'\frac{\partial f}{\partial\xi}\right], \end{aligned} \tag{11}$$

$$\frac{1}{Sc}\left[\phi'' + \frac{N_T}{N_B}\theta''\right] + f\phi' + S_r\,\theta'' = \xi\left[f'\frac{\partial\phi}{\partial\xi} - \phi'\frac{\partial f}{\partial\xi}\right]. \tag{12}$$

the transformed boundary conditions emerge as:

$$\left.\begin{array}{ll} f = f' = 0, \quad \theta = \phi = 1 & \text{at } \eta = 0, \\ f' \to 0, \qquad \theta \to 0, \quad \phi \to 0 & \text{as } \eta \to \infty. \end{array}\right\} \tag{13}$$

where $Gr = \frac{a^3 \rho_{f\infty}(1-C_\infty) g_a \beta_1 (T_W - T_\infty)}{\nu_f^2}$, $We = \frac{\Gamma \nu_f \sqrt{2} (Gr)^{3/4}}{a^2}$, $\Pr = \frac{\mu_f (C_p)_f}{k_f}$, $M_a = \frac{\sigma a^2 B_0}{(Gr)^{1/2} \nu_f \rho_f}$, $N_r = \frac{(\rho_p - \rho_f)(C_W - C_\infty)}{(1-C_\infty)\rho_f \beta_1 (T_W - T_\infty)}$, $\gamma^* = \gamma (T_W - T_\infty)$, $N_B = \frac{\tau D_B (C_W - C_\infty)}{\nu_f}$, $R_a = \frac{k_e k_f}{4\sigma_B T_\infty^3}$, $N_T = \frac{\tau D_T (T_W - T_\infty)}{\nu_f T_\infty}$, $\delta^* = \delta (T_W - T_\infty)$, $D_u = \frac{D_B K_T (C_W - C_\infty)}{\nu_f C_S (C_p)_f (T_W - T_\infty)}$, $S_r = \frac{D_B K_T (T_W - T_\infty)}{\nu T_m (C_W - C_\infty)}$ and $Sc = \frac{\nu_f}{D_B}$.

At the wall, dimensional forms of skin friction factor (C_f), heat transfer rate (Nu^*) and mass transfer rate (Sh^*) are expressed as follows:

$$C_f = \tau_w, \quad Nu^* = \frac{-a\, q_w}{k_f (T_w - T_\infty)}, \quad Sh^* = \frac{-a\, J_w}{D_B (C_w - C_\infty)}. \tag{14}$$

where, $\tau_w = \mu (T) \left[\frac{\partial u}{\partial y} + \frac{\Gamma}{2} \left(\frac{\partial u}{\partial y} \right)^2 \right]_{y=0}$, $q_w = k (T) \left[\frac{\partial T}{\partial y} \right]_{y=0} + (q_r)_{y=0}$,

$$J_w = D_B \left[\frac{\partial C}{\partial y} \right]_{y=0}.$$

by employing τ_w, q_w and J_w in Equ. 14, then Equ. 14 can be written as

$$\left.\begin{array}{l} C_f = \mu (T) \left[\frac{\partial u}{\partial y} + \frac{\Gamma}{2} \left(\frac{\partial u}{\partial y} \right)^2 \right]_{y=0}, \\ Nu^* = \frac{-a \left(k(T) \left[\frac{\partial T}{\partial y} \right]_{y=0} + (q_r)_{y=0} \right)}{k_f (T_w - T_\infty)}, \\ Sh^* = \frac{-a \left[\frac{\partial C}{\partial y} \right]_{y=0}}{(C_w - C_\infty)}. \end{array}\right\} \tag{15}$$

In non-dimensional, skin friction $\left(C_f^* \right)$, heat transfer rate (Nu^*) and mass transfer rate (Sh^*) can be written as

$$\left.\begin{array}{l} C_f^* \left(Gr^{-3/4} \right) = (1 - \gamma^* \theta)\, f'' (0)\, \xi \left(1 + \xi \frac{We}{\sqrt{2}} f'' (0) \right), \\ Nu^* \left(Gr^{-1/4} \right) = - \left((1 + \delta^* \theta) + \frac{4}{3R_a} \right) \theta' (0), \\ Sh^* \left(Gr^{-1/4} \right) = -\phi' (0). \end{array}\right\} \tag{16}$$

where, $C_f^* = \frac{C_f a^2}{\mu_f \nu_f}$.

3. Numerical method

Keller box method (KBM) which is introduced by Keller (1971). This method is initially applied to solve parabolic problems. Later, this scheme is applied to solve various problems in laminar and turbulent boundary layer flows. The notable merits of this scheme are:

- This scheme is well-organized, simple and flexible to program.
- In this scheme, there is no need to formulate any conditions to compute very close to the point of boundary layer separation.
- The variations in streamwise coordinate (ξ-direction) are rapidly admitted.
- The scheme has second-order accuracy and unconditionally stable.
- The non-similar solutions are obtained for boundary layer flow problems.

The similarity solution merely depends on the free stream velocity for the boundary layer equations. But the boundary layers may arise from various factors like the variation in wall temperature, free-stream velocity, suction/injection of fluid at the wall, and buoyancy effect. The non-similar solution can account these effects in the boundary layer. In addition, there is no clarity for ignoring certain streamwise derivatives in the similarity solution when converting the governing equations into dimensionless form. This dilutes the accuracy of the solutions. In a non-similar solution, only the auxiliary equations are removed from the fluid transport equations. Thus the original fluid transport equations with boundary conditions remain same. Hence, it is expected that the non-similar solutions can provide more accurate results than the local-similarity solution. The procedure to obtain the solution by using the Keller box method is given below

- The n^{th} order dimensionless equations are transformed into n first order dimensionless equations.
- The transformed n first order equations are discretized by employing central differences approach.
- The algebraic equations are linearized by means of Newton's method.
- The results are obtained by solution of the block matrix system (block tri-diagonal elimination technique).

Step 1:

We consider a new set of variables $u(\xi,\eta), v(\xi,\eta), s(\xi,\eta), t(\xi,\eta), g(\xi,\eta), p(\xi,\eta)$ to transform the n^{th} order dimensionless equations into the first order dimensionless equations, which depends on ξ and η.

The new set of variables are assumed as

$$f = f, f' = u,\ u' = v, \theta = s,\ s' = t, \phi = g,\ g' = p, \tag{17}$$

By implementing the above variables, Eqs. (10)-(12) are transformed to

$$(1-\gamma^* s)\,v' + 2We\xi\,(1-\gamma^* s)\,v'v - We\xi\gamma^*(v)^2 t - \gamma^* vs \tag{18}$$
$$-(u)^2 + fv + B\,(s - N_r g) - M_a u = \xi\left[u\frac{\partial u}{\partial \xi} - v\frac{\partial f}{\partial \xi}\right]$$

$$\frac{1}{\Pr}\left[(1+\delta^* s) + \frac{4}{3R_a}\right]t' + \frac{\delta^*(t)^2}{\Pr} + ft + N_B tp \tag{19}$$
$$+N_T(t)^2 + D_u\,p' = \xi\left[u\frac{\partial s}{\partial \xi} - t\frac{\partial f}{\partial \xi}\right]$$

$$\frac{1}{Sc}\left[p' + \frac{N_T}{N_B}t'\right] + fp + S_r\,t' = \xi\left[u\frac{\partial g}{\partial \xi} - p\frac{\partial f}{\partial \xi}\right] \tag{20}$$

with the boundary conditions

$$\eta = 0: \quad u = 0, \quad f = 0, \quad s = 1, \quad g = 1 \tag{21}$$
$$\eta \to \infty: \quad u = 0, \quad s = 0, \quad g = 0$$

Step 2:

The net point on the (ξ, η) plane is expressed using the following relations:

$$\xi^0 = 0, \quad \xi^i = \xi^{i-1} + k_i, \; i = 1, 2, 3...I, \tag{22}$$
$$\eta_0 = 0, \quad \eta_j = \eta_{j-1} + h_j, \; j = 1, 2, 3...J. \tag{23}$$

where k_i is $\Delta\xi$ spacing at the i^{th} node and h_j is $\Delta\eta$ spacing at j^{th} node. The following discretizations are applied:

$$\left(\frac{\partial()}{\partial\xi}\right)^{i-\frac{1}{2}}_{j-\frac{1}{2}} = \frac{()^i_{j-\frac{1}{2}} - ()^{i-1}_{j-\frac{1}{2}}}{k_i}, \quad \left(\frac{\partial()}{\partial\eta}\right)^{i-\frac{1}{2}}_{j-\frac{1}{2}} = \frac{()^{i-\frac{1}{2}}_{j} - ()^{i-\frac{1}{2}}_{j-1}}{h_j}$$
$$()^{i-\frac{1}{2}}_{j} = \frac{()^{i-1}_{j} - ()^{i}_{j}}{2}, \quad ()^{i}_{j-\frac{1}{2}} = \frac{()^{i}_{j-1} - ()^{i}_{j}}{2}$$

At the midpoint $\left(\xi^i, \eta_{j-\frac{1}{2}}\right)$ between the segments $\left(\xi^i, \eta_{j-1}\right)\left(\xi^i, \eta_j\right)$ the following central difference approximations are deployed:

$$f' = u \Rightarrow u^i_{j-\frac{1}{2}} = \frac{u^i_j + u^i_{j-1}}{2} = \frac{\left(f^i_j - f^i_{j-1}\right)}{h_j}, \tag{24}$$

$$u' = v \Rightarrow v^i_{j-\frac{1}{2}} = \frac{v^i_j + v^i_{j-1}}{2} = \frac{\left(u^i_j - u^i_{j-1}\right)}{h_j}, \tag{25}$$

$$s' = t \Rightarrow t^i_{j-\frac{1}{2}} = \frac{t^i_j + t^i_{j-1}}{2} = \frac{\left(s^i_j - s^i_{j-1}\right)}{h_j}, \tag{26}$$

$$g' = p \Rightarrow p^i_{j-\frac{1}{2}} = \frac{p^i_j + p^i_{j-1}}{2} = \frac{\left(g^i_j - g^i_{j-1}\right)}{h_j}, \tag{27}$$

First order PDEs (16) to (18) are approximated by centering at $\left(\xi^{i-\frac{1}{2}}, \eta_{j-\frac{1}{2}}\right)$ from the rectangle points ($P_1, P_2, P_3,$ and P_4) giving the following equations:

$$\left.\begin{array}{l}
\left(\frac{v^i_j - v^i_{j-1}}{h_j}\right) - \gamma^* s^i_{j-1/2}\left(\frac{v^i_j - v^i_{j-1}}{h_j}\right) + 2We\xi v^i_{j-1/2}\left(\frac{v^i_j - v^i_{j-1}}{h_j}\right) \\
-2We\xi\gamma^* s^i_{j-1/2} v^i_{j-1/2}\left(\frac{v^i_j - v^i_{j-1}}{h_j}\right) - We\xi\gamma^* t^i_{j-1/2}\left(v^i_{j-1/2}\right)^2 \\
-\gamma^*\left(t^i_{j-1/2} v^i_{j-1/2}\right) + (1+\alpha)\left(f^i_{j-1/2} v^i_{j-1/2}\right) - (1+\alpha)\left(u^i_{j-1/2}\right)^2 \\
-(M_a)\, u^i_{j-1/2} + \alpha v^{i-1}_{j-1/2} f^i_{j-1/2} - \alpha f^{i-1}_{j-1/2} v^i_{j-1/2} + B\left(s^i_{j-1/2} - N_r g^i_{j-1/2}\right) \\
= -\left[\begin{array}{l}
\left(\frac{v^i_j - v^i_{j-1}}{h_j}\right) - \gamma^* s^i_{j-1/2}\left(\frac{v^i_j - v^i_{j-1}}{h_j}\right) + 2We\xi v^i_{j-1/2}\left(\frac{v^i_j - v^i_{j-1}}{h_j}\right) \\
-2We\xi\gamma^* s^i_{j-1/2} v^i_{j-1/2}\left(\frac{v^i_j - v^i_{j-1}}{h_j}\right) - We\xi\gamma^* t^i_{j-1/2}\left(v^i_{j-1/2}\right)^2 \\
-\gamma^*\left(t^i_{j-1/2} v^i_{j-1/2}\right) + (1-\alpha)\left(f^{i-1}_{j-1/2} v^{i-1}_{j-1/2}\right) + (\alpha - 1) \\
\left(u^{i-1}_{j-1/2}\right)^2 + B\left(s^{i-1}_{j-1/2} - N_r g^{i-1}_{j-1/2}\right) - (M_a)\, u^{i-1}_{j-1/2}
\end{array}\right]
\end{array}\right\} \tag{28}$$

$$\left.\begin{array}{l}
\frac{1}{\mathrm{Pr}}\left[1 + \frac{4}{3R_a}\right]\left(\frac{t^i_j - t^i_{j-1}}{h_j}\right) + \frac{\delta^*}{\mathrm{Pr}} s^i_{j-1/2}\left(\frac{t^i_j - t^i_{j-1}}{h_j}\right) \\
+\frac{\delta^*}{\mathrm{Pr}}\left(t^i_{j-1/2}\right)^2 + N_B\left(t^i_{j-1/2} p^i_{j-1/2}\right) + N_T\left(t^i_{j-1/2}\right)^2 \\
+D_u\left(\frac{p^i_j - p^i_{j-1}}{h_j}\right) - \alpha u^{i-1}_{j-1/2} s^i_{j-1/2} - \alpha f^{i-1}_{j-1/2} t^i_{j-1/2} \\
+\alpha t^{i-1}_{j-1/2} f^i_{j-1/2} + (1+\alpha)\left(f^i_{j-1/2} t^i_{j-1/2}\right) \\
-\alpha\left(u^i_{j-1/2} s^i_{j-1/2}\right) + \alpha s^{i-1}_{j-1/2} u^i_{j-1/2} \\
= -\left[\begin{array}{l}
\frac{1}{\mathrm{Pr}}\left[1 + \frac{4}{3R_a}\right]\left(\frac{t^i_j - t^i_{j-1}}{h_j}\right) + \frac{\delta^*}{\mathrm{Pr}} s^i_{j-1/2}\left(\frac{t^i_j - t^i_{j-1}}{h_j}\right) \\
+\frac{\delta^*}{\mathrm{Pr}}\left(t^i_{j-1/2}\right)^2 + N_B\left(t^i_{j-1/2} p^i_{j-1/2}\right) \\
+N_T\left(t^i_{j-1/2}\right)^2 + D_u\left(\frac{p^i_j - p^i_{j-1}}{h_j}\right) \\
+(1-\alpha)\left(f^{i-1}_{j-1/2} t^{i-1}_{j-1/2}\right) + \alpha\left(u^{i-1}_{j-1/2} s^{i-1}_{j-1/2}\right)
\end{array}\right]
\end{array}\right\} \tag{29}$$

$$\left.\begin{array}{l}
\frac{1}{Sc}\left(\frac{p^i_j - p^i_{j-1}}{h_j}\right) + \frac{1}{Sc}\left(\frac{N_T}{N_B}\right)\left(\frac{t^i_j - t^i_{j-1}}{h_j}\right) + S_r\left(\frac{t^i_j - t^i_{j-1}}{h_j}\right) \\
+(1+\alpha)\left(f^i_{j-1/2} p^i_{j-1/2}\right) - \alpha\left(u^i_{j-1/2} g^i_{j-1/2}\right) + \alpha g^{i-1}_{j-1/2} u^i_{j-1/2} \\
-\alpha u^{i-1}_{j-1/2} g^i_{j-1/2} - \alpha f^{i-1}_{j-1/2} p^i_{j-1/2} + \alpha p^{i-1}_{j-1/2} f^i_{j-1/2} \\
= -\left[\begin{array}{l}
\frac{1}{Sc}\left(\frac{p^i_j - p^i_{j-1}}{h_j}\right) + \frac{1}{Sc}\left(\frac{N_T}{N_B}\right)\left(\frac{t^i_j - t^i_{j-1}}{h_j}\right) + S_r\left(\frac{t^i_j - t^i_{j-1}}{h_j}\right) \\
+(1-\alpha)\left(f^{i-1}_{j-1/2} p^{i-1}_{j-1/2}\right) + \alpha\left(u^{i-1}_{j-1/2} g^{i-1}_{j-1/2}\right)
\end{array}\right]
\end{array}\right\} \tag{30}$$

where $\alpha = \frac{\xi^{n-1/2}}{k_n}$, $B = \frac{\sin\left(\xi^{n-1/2}\right)}{\xi^{n-1/2}}$

The boundary conditions become

$$f_0^i = u_0^i = 0,\ s_0^i = 1,\ g_0^i = 1,\ u_J^i = 0,\ s_J^i = 0,\ g_J^i = 0 \tag{31}$$

Step 3:

The unknowns $(f_j^i,\ u_j^i,\ v_j^i,\ g_j^i,\ p_j^i,\ s_j^i,\ t_j^i)$ are calculated with help of following knowns $f_j^{i-1},\ u_j^{i-1}, v_j^{i-1}, g_j^{i-1}, p_j^{i-1}, s_j^{i-1}, t_j^{i-1}$ where 0 ≤ j ≤ J and $(f_j^i,\ u_j^i,\ v_j^i,\ g_j^i,\ p_j^i,\ s_j^i,\ t_j^i) \equiv (f_j,\ u_j,\ v_j,\ g_j,\ p_j,\ s_j,\ t_j)$.

The set of central difference equations can be expressed as

$$\frac{u_j + u_{j-1}}{2} = \frac{f_j - f_{j-1}}{h_j}, \tag{32}$$

$$\frac{v_j + v_{j-1}}{2} = \frac{u_j - u_{j-1}}{h_j}, \tag{33}$$

$$\frac{t_j + t_{j-1}}{2} = \frac{s_j - s_{j-1}}{h_j}, \tag{34}$$

$$\frac{p_j + p_{j-1}}{2} = \frac{g_j - g_{j-1}}{h_j}, \tag{35}$$

$$\left.\begin{array}{l}
(v_j - v_{j-1}) - \frac{\gamma^*}{2}(s_j + s_{j-1})(v_j - v_{j-1}) + We\xi(v_j + v_{j-1})(v_j - v_{j-1}) \\
-\frac{We\xi\gamma^*}{2}(s_j + s_{j-1})(v_j + v_{j-1})(v_j - v_{j-1}) - \frac{We\xi h_j\gamma^*}{8}(t_j + t_{j-1}) \\
(v_j + v_{j-1})^2 + \frac{(1+\alpha)h_j}{4}[(f_j + f_{j-1})(v_j + v_{j-1})] - \frac{h_j}{4}(1+\alpha) \\
(u_j + u_{j-1})^2 - \frac{\gamma^*}{4}h_j(v_j + v_{j-1})(t_j + t_{j-1}) - \frac{h_j}{2}(M_a)(u_j + u_{j-1}) \\
+\frac{\alpha h_j}{2}v_{j-1/2}^{i-1}(f_j + f_{j-1}) - \frac{\alpha h_j}{2}f_{j-1/2}^{i-1}(v_j + v_{j-1}) \\
+\frac{Bh_j}{2}[s_j + s_{j-1} - N_r(g_j + g_{j-1})] = [E_1]_{j-1/2}^{i-1}
\end{array}\right\} \tag{36}$$

$$\left.\begin{array}{l}
\frac{1}{\mathrm{Pr}}\left[1 + \frac{4}{3R_a}\right](t_j - t_{j-1}) + \frac{\delta^*}{2\,\mathrm{Pr}}(s_j + s_{j-1})(t_j - t_{j-1}) \\
+\frac{\delta^*}{4\,\mathrm{Pr}}h_j(t_j + t_{j-1})^2 + \frac{N_B}{4}h_j(t_j + t_{j-1})(p_j + p_{j-1}) \\
+\frac{N_T}{4}h_j(t_j + t_{j-1})^2 + D_u(p_j - p_{j-1}) + \frac{(1+\alpha)h_j}{4}(f_j + f_{j-1}) \\
(t_j + t_{j-1}) - \frac{\alpha h_j}{4}[(u_j + u_{j-1})(s_j + s_{j-1})] \\
+\frac{\alpha h_j}{2}s_{j-1/2}^{i-1}(u_j + u_{j-1}) - \frac{\alpha h_j}{2}u_{j-1/2}^{i-1}(s_j + s_{j-1}) \\
-\frac{\alpha h_j}{2}f_{j-1/2}^{i-1}(t_j + t_{j-1}) + \frac{\alpha h_j}{2}t_{j-1/2}^{i-1}(f_j + f_{j-1}) = [E_2]_{j-1/2}^{i-1}
\end{array}\right\} \tag{37}$$

$$\left.\begin{array}{l}
\frac{1}{Sc}(p_j - p_{j-1}) + \frac{1}{Sc}\frac{N_T}{N_B}(t_j - t_{j-1}) + S_r(t_j - t_{j-1}) \\
+\frac{(1+\alpha)h_j}{4}[(f_j + f_{j-1})(p_j + p_{j-1})] - \frac{\alpha h_j}{4}[(u_j + u_{j-1})(g_j + g_{j-1})] \\
+\frac{\alpha h_j}{2}g_{j-1/2}^{i-1}(u_j + u_{j-1}) - \frac{\alpha h_j}{2}u_{j-1/2}^{i-1}(g_j + g_{j-1}) \\
-\frac{\alpha h_j}{2}f_{j-1/2}^{i-1}(p_j + p_{j-1}) + \frac{\alpha h_j}{2}p_{j-1/2}^{i-1}(f_j + f_{j-1}) = [E_3]_{j-1/2}^{i-1}
\end{array}\right\} \tag{38}$$

$$[E_1]_{j-1/2}^{i-1} = -h_j \begin{bmatrix} \left(\frac{v_j - v_{j-1}}{h_j}\right) - \gamma^* s_{j-1/2}\left(\frac{v_j - v_{j-1}}{h_j}\right) + 2We\xi v_{j-1/2} \\ \left(\frac{v_j - v_{j-1}}{h_j}\right) - 2We\xi\gamma^* s_{j-1/2} v_{j-1/2}\left(\frac{v_j - v_{j-1}}{h_j}\right) \\ -We\xi\gamma^* t_{j-1/2}\left(v_{j-1/2}\right)^2 - \gamma^*\left(t_{j-1/2} v_{j-1/2}\right) \\ +(1-\alpha)\left(f_{j-1/2} v_{j-1/2}\right) + (\alpha - 1)\left(u_{j-1/2}\right)^2 \\ +B\left(s_{j-1/2} - N_r g_{j-1/2}\right) - (M_a)\, u_{j-1/2} \end{bmatrix} \tag{39}$$

$$[E_2]_{j-1/2}^{i-1} = -h_j \begin{bmatrix} \frac{1}{\mathrm{Pr}}\left[1 + \frac{4}{3R_a}\right]\left(\frac{t_j - t_{j-1}}{h_j}\right) + \frac{\delta^*}{\mathrm{Pr}} s_{j-1/2}\left(\frac{t_j - t_{j-1}}{h_j}\right) \\ +\frac{\delta^*}{\mathrm{Pr}}\left(t_{j-1/2}\right)^2 + N_B\left(t_{j-1/2} p_{j-1/2}\right) \\ +N_T\left(t_{j-1/2}\right)^2 + D_u\left(\frac{p_j - p_{j-1}}{h_j}\right) \\ +(1-\alpha)\left(f_{j-1/2} t_{j-1/2}\right) + \alpha\left(u_{j-1/2} s_{j-1/2}\right) \end{bmatrix} \tag{40}$$

$$[E_3]_{j-1/2}^{i-1} = -h_j \begin{bmatrix} \frac{1}{Sc}\left(\frac{p_j - p_{j-1}}{h_j}\right) + \frac{1}{Sc}\left(\frac{N_T}{N_B}\right)\left(\frac{t_j - t_{j-1}}{h_j}\right) + \\ S_r\left(\frac{t_j - t_{j-1}}{h_j}\right) + (1-\alpha)\left(f_{j-1/2} p_{j-1/2}\right) \\ +\alpha\left(u_{j-1/2} g_{j-1/2}\right) \end{bmatrix} \tag{41}$$

Here $[E_1]_{j-1/2}^{i-1}$, $[E_2]_{j-1/2}^{i-1}$ and $[E_3]_{j-1/2}^{i-1}$ are the known quantities

Linearization and block elimination processes of KBM scheme have provided in the appendix section.

In the present problem, the maximum values of ξ and η considered as 1 and 30, respectively. The difference between the spatial nodes are taken as 0.05 in both directions for convergence of the solution. It is noteworthy to mention that the pseudoplastic nanofluid boundary layer regime is meshed with a (20×600) grid. To increase the accuracy of the present solution the convergence criterion has been fixed as 10^{-6} at all grid points. Comparison results of Nu^* for various values of streamwise coordinate, ξ, are provided in Table 1. It is evident that the current Keller box solutions achieve a very good agreement with the results obtained by Merkin (1977), Yih (2000) and Prasad et al. (2019) when nanoscale and other effects are neglected to reduce the current boundary value problem to exactly that considered by these earlier studies with exactly the same data prescribed. It is witnessed that the obtained Keller box code is therefore justifiably very high. Tables 2, 3 and 4 documents the Keller box solutions for skin friction factor, rates of heat and mass transfer with diverse values in key parameters. These tables provide a useful benchmark for future researchers to validate alternative numerical computations with supplementary multi-physical effects against. Fig. 2 illustrates the Keller box numerical methodology, boundary layer mesh and Keller box discretization process.

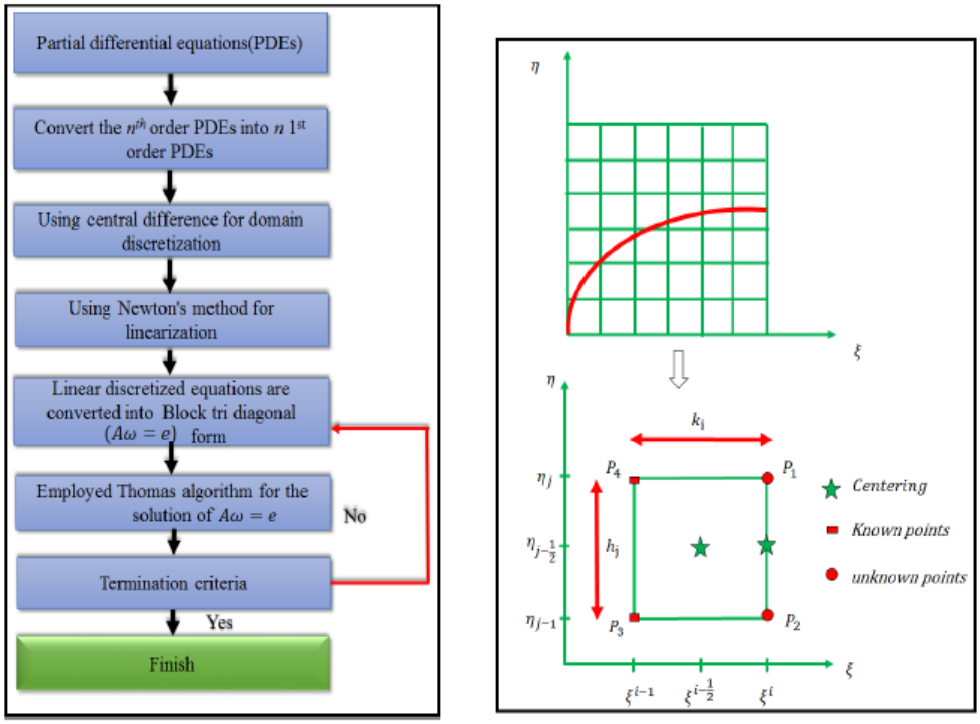

Fig. 2. Solution approach by computer, boundary layer mesh and Keller box element .

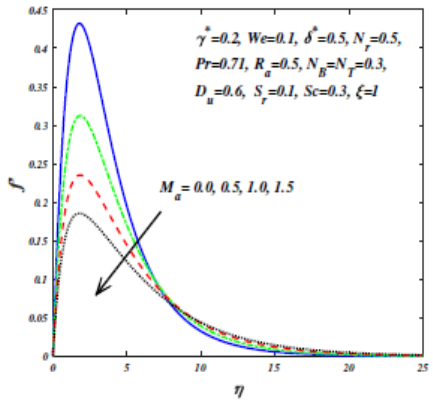

Fig. 3. f' for uplifting values of M_a.

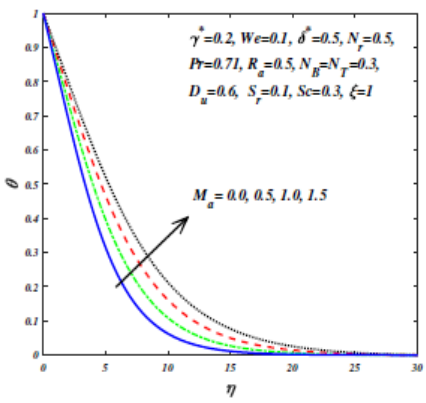

Fig. 4. θ for uplifting values of M_a.

4. Results and discussion

The current section is aimed to visualize the influence of emerging parameters on velocity (f'), temperature (θ), concentration (ϕ), skin friction factor (C_f^*), wall heat transfer rate (Nu^*) and wall nanoparticle mass transfer rate (Sh^*). The parame-

Table 1. Comparison result of Nu for various values of ξ with Pr=0.71, $R_a \to \infty$, M_a=0.5, Sc=0.6, We=N_r=γ^*=δ^*=N_B=N_T=D_u=S_r=0

ξ	$Nu^*\left(Gr^{-1/4}\right) = -\theta'(\xi, 0)$			
	Merkin(1977)	Yih(2000)	Prasad et al.(2019)	Present
0.0	0.4212	0.4214	0.4211	0.4211
0.2	0.4204	0.4207	0.4206	0.4206
0.4	0.4182	0.4184	0.4185	0.4185
0.6	0.4145	0.4147	0.4146	0.4146
0.8	0.4093	0.4096	0.4095	0.4095
1.0	0.4025	0.4030	0.4027	0.4027
1.2	0.3942	0.3950	0.3947	0.3947
1.4	0.3843	0.3854	0.3852	0.3852
1.6	0.3727	0.3740	0.3735	0.3735
1.8	0.3594	0.3608	0.3598	0.3598
2.0	0.3443	0.3457	0.3448	0.3448
2.2	0.3270	0.3283	0.3280	0.3280
2.4	0.3073	0.3086	0.3076	0.3076
2.6	0.2847	0.2860	0.2852	0.2852
2.8	0.2581	0.2595	0.2592	0.2592
3.0	0.2252	0.2267	0.2255	0.2255
π	0.1963	0.1962	0.1961	0.1961

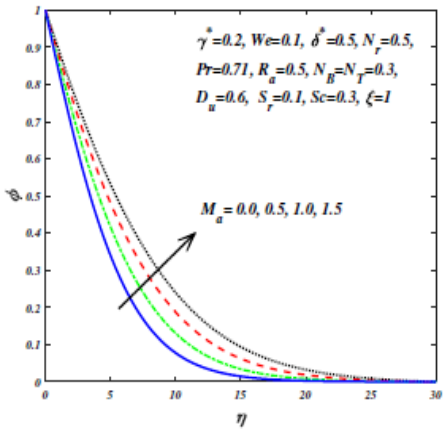

Fig. 5. ϕ for uplifting values of M_a.

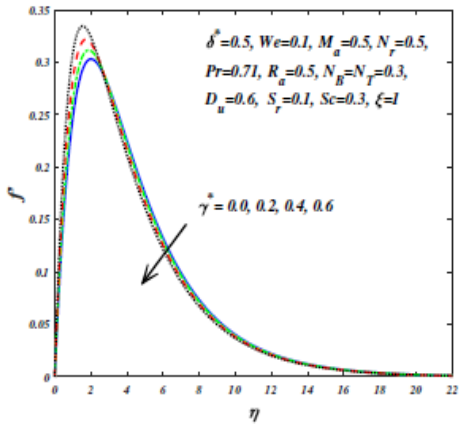

Fig. 6. f' for uplifting values of γ^*.

ters varied and their ranges are: Weissenberg number ($We = 0, 0.5, 1, 1.5$), magnetic field ($M_a = 0.0, 0.5, 1.0, 1.5$), variable viscosity parameter ($\gamma^* = 0.0, 0.2, 0.4, 0.6$), variable thermal conductivity parameter ($\delta^* = 0.0, 0.5, 1.0, 1.5$), Brownian motion ($N_B = 0.2, 0.4, 0.6, 0.8$), thermophoresis ($N_T = 0.01, 0.1, 0.3, 0.5$), radiation

Table 2. Impacts of γ^* and δ^* on local skin friction coefficient $\left(C_f^*(Gr^{-3/4})\right)$, dimensionless local rate of heat transfer $\left(Nu^*(Gr^{-1/4})\right)$ and dimensionless local rate of mass transfer$\left(Sh^*(Gr^{-1/4})\right)$ for various values of ξ

Physical Parameters	Values	Physical Quantities	ξ						CPU time(Sec.)
			0	0.5	1	1.5	2	2.5	
γ^*	0	$C_f^*(Gr^{-3/4})$	0	0.2284	0.4048	0.4779	0.4482	0.2708	8.365484
		$Nu^*(Gr^{-1/4})$	0.5761	0.5590	0.5271	0.4757	0.4055	0.3013	
		$Sh^*(Gr^{-1/4})$	0.1523	0.1479	0.1395	0.1261	0.1078	0.0804	
	0.2	$C_f^*(Gr^{-3/4})$	0	0.2006	0.3612	0.4178	0.4047	0.2421	8.061629
		$Nu^*(Gr^{-1/4})$	0.5839	0.5645	0.5338	0.4802	0.4118	0.3056	
		$Sh^*(Gr^{-1/4})$	0.1542	0.1492	0.1411	0.1272	0.1093	0.0814	
	0.4	$C_f^*(Gr^{-3/4})$	0	0.1667	0.3059	0.3479	0.3433	0.2156	9.043056
		$Nu^*(Gr^{-1/4})$	0.5933	0.5701	0.5414	0.4850	0.4186	0.3118	
		$Sh^*(Gr^{-1/4})$	0.1564	0.1504	0.1430	0.1283	0.1109	0.0830	
	0.6	$C_f^*(Gr^{-3/4})$	0	0.1466	0.2719	0.3077	0.3046	0.1996	12.654024
		$Nu^*(Gr^{-1/4})$	0.5987	0.5728	0.5455	0.4877	0.4221	0.3158	
		$Sh^*(Gr^{-1/4})$	0.1577	0.1510	0.1439	0.1289	0.1118	0.0839	
δ^*	0	$C_f^*(Gr^{-3/4})$	0	0.1962	0.3529	0.4081	0.3948	0.2354	8.193623
		$Nu^*(Gr^{-1/4})$	0.5469	0.5286	0.4996	0.4490	0.3844	0.2839	
		$Sh^*(Gr^{-1/4})$	0.1400	0.1355	0.1281	0.1154	0.0989	0.0735	
	0.5	$C_f^*(Gr^{-3/4})$	0	0.2006	0.3612	0.4178	0.4047	0.2421	8.239927
		$Nu^*(Gr^{-1/4})$	0.5839	0.5645	0.5338	0.4802	0.4118	0.3056	
		$Sh^*(Gr^{-1/4})$	0.1542	0.1492	0.1411	0.1272	0.1093	0.0814	
	1.0	$C_f^*(Gr^{-3/4})$	0	0.2045	0.3683	0.4261	0.4132	0.2480	8.099395
		$Nu^*(Gr^{-1/4})$	0.6198	0.5993	0.5669	0.5104	0.4384	0.3268	
		$Sh^*(Gr^{-1/4})$	0.1657	0.1603	0.1518	0.1368	0.1178	0.0880	
	1.5	$C_f^*(Gr^{-3/4})$	0	0.2077	0.3744	0.4333	0.4206	0.2532	9.210965
		$Nu^*(Gr^{-1/4})$	0.6546	0.6332	0.5991	0.5398	0.4642	0.3474	
		$Sh^*(Gr^{-1/4})$	0.1753	0.1695	0.1606	0.1448	0.1249	0.0935	

($R_a = 0.1, 0.3, 0.5, 0.8$), Soret number ($S_r = 0.4, 0.2, 0.1, 0.075$), and Dufour number ($D_u = 0.15, 0.3, 0.6, 0.8$). All data utilized in the simulations is based on practically viable nano-materials processing systems and extracted from Das et al. (2007) and Jaluria (2013). Figures 3-22 depict the variation in momentum, heat and nanoparticle concentration characteristics and consistently smooth profiles are achieved in the free stream, testifying to the prescription of an adequately larger infinity boundary condition. A further novelty in the current study is that Figs. 23-25 have been included to visualize the 3-D contour distributions and Figs. 26-28 have been provided to illustrate the streamline, isothermal and iso-concentration distributions. This colour contoured visualization has invariably been omitted in the majority of

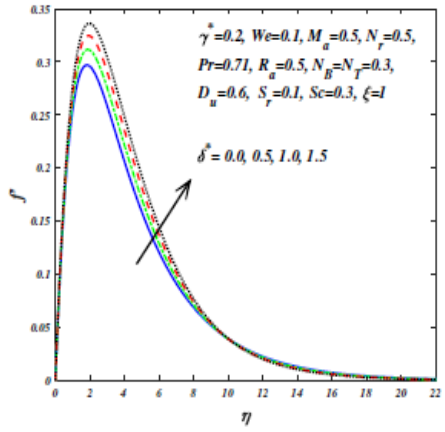

Fig. 7. f' for uplifting values of δ^*.

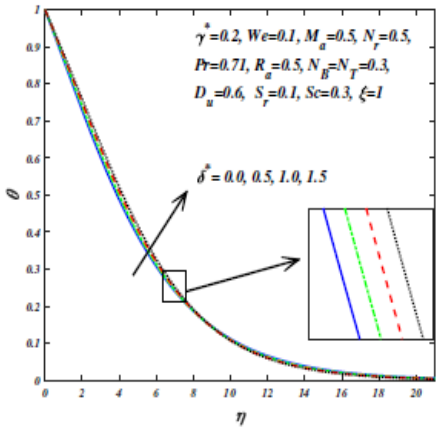

Fig. 8. θ for uplifting values of δ^*.

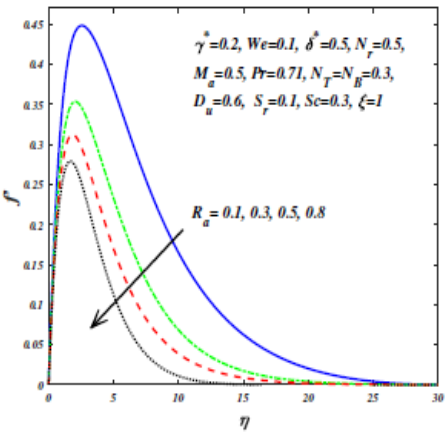

Fig. 9. f' for uplifting values of R_a.

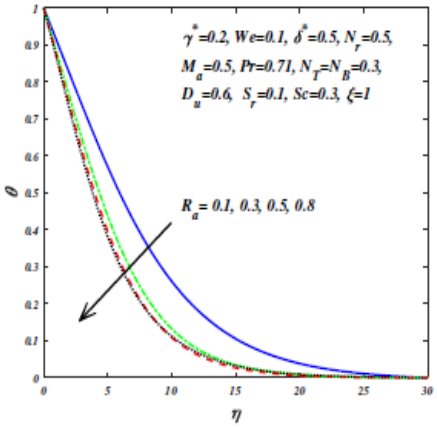

Fig. 10. θ for uplifting values of R_a.

Keller box numerical studies.

The impact of magnetic field (M_a) on velocity (f'), temperature (θ) and nanoparticle concentration (ϕ) are depicted in Figs. 3-5. In an electrically conducting fluid (e.g. magnetic nano-polymer), the magnetic field (B_0) applied in the transverse direction creates an orthogonal hydromagnetic retarding force (Lorentz force) which resists the fluid motion. The magnitude of Lorentz force increases with magnetic field, B_0, which acts to significantly reduce the velocity of nanofluid. Momentum (hydrodynamic) related boundary layer thickness is therefore enhanced by employing stronger magnetic field. The implication is that regulation in coating flow of the magnetic nano-polymer is achieved successfully via a boost in radial magnetic field which permits more homogenous distribution of the nano-polymer over the cylinder periphery. The classical velocity overshoot arising in close proximity to

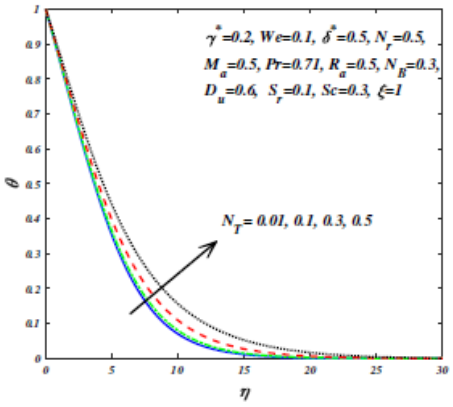

Fig. 11. θ for uplifting values of N_T.

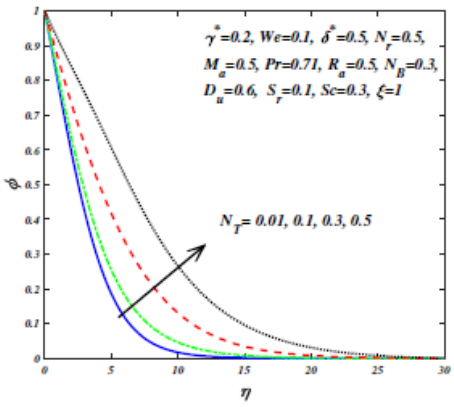

Fig. 12. ϕ for uplifting values of N_T.

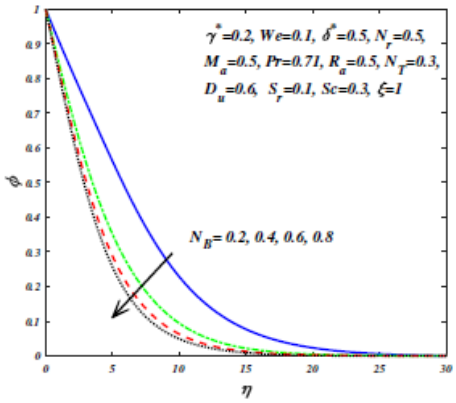

Fig. 13. ϕ for uplifting values of N_B.

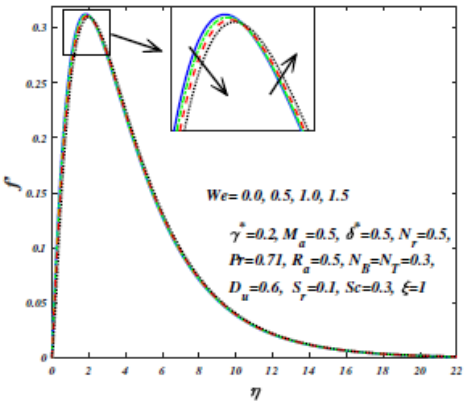

Fig. 14. f' for uplifting values of We.

the wall (cylinder surface) is also clearly captured and is progressively suppressed with greater values of M_a. Maximum acceleration and thinnest boundary layer thickness corresponds to the electrically non-conducting case ($M_a = 0$). Although a slight switch in the effect of magnetic field on velocity distribution is generated further from the cylinder surface (approaching the free stream), the dominant effect is retardation. However back flow is never instigated since velocities are consistently positive indicating that even at relatively strong magnetic field ($M_a = 1.5$), flow separation is avoided. The evolutions in temperature and nano-particle concentration with magnetic field are displayed in Figs. 4 and 5, respectively. Strengthening the magnetic field results in enhanced Lorentz force which necessitates greater work expenditure by the nanofluid in dragging against the action of the magnetic field. This excess work is dissipated as thermal energy which heats the coating regime and elevates thermal boundary layer thickness. A consistently monotonic decay

in temperatures from the cylinder surface to the free stream is computed (Fig. 4). Simultaneously the nanoparticle diffusion is assisted in the boundary layer i.e. nanoparticle concentration magnitudes (Fig. 5) are boosted as is the nanoparticle concentration boundary layer thickness. Magnetic field therefore has the dual benefit of flow control and mobilization of more homogenous migration of nanoparticles; however, it leads to temperature elevation.

The response in velocity distribution to variable viscosity parameter (γ^*) is given in Fig. 6. γ^* takes positive values to characterize the water, crude oil, and benzene whereas it takes negative values to represent air, methane, and helium. It is apparent that increasing the viscosity of Williamson fluid initially slightly increases the velocity near the cylinder surface (wall); however the dominant effect is a deceleration which extends through the majority of the boundary layer region and is attributable to the reduction in momentum diffusion with larger viscosity. A similar response has been reported by Kafoussias and Williams (1995) and Nasrin and Alim (2009), among many other studies. Figures 7 and 8 exhibit the influence of variable thermal conductivity parameter δ^* on nanofluid velocity and temperature. It is evident from these figures that both characteristics manifest an elevation with higher values of δ^*. This parameter features in the augmented thermal diffusion term, $1/\mathrm{Pr}\,(1+\delta^*\theta)\theta''$ in the energy eqn. (11) and accentuates heat transfer inside the nanofluid. The greater thermal conductivity of the nanofluid intensifies thermal conduction which assists also in thermal diffusion and momentum diffusion. This results in a decrease in hydrodynamic boundary layer thickness and accentuation in thermal boundary layer thickness. Evidently the inclusion of thermal conductivity variation produces results which more accurately predict the velocity and temperature magnitudes. Absence of this parameter (δ^*=0) leads to an under-prediction in both quantities and higher momentum and lower thermal boundary layer thickness estimates, which are undesirable in manufacturing operations and can incur expenses, as noted by Jaluria (2013).

Figures 9 and 10 depict the influence of Rossleand conduction-radiation parameter (R_a) on fluid velocity and temperature profiles, respectively. As with the thermal conductivity variation parameter, δ^*, the Rossleand conduction-radiation parameter $R_a = \frac{k_e k_f}{4\sigma_B T_\infty^3}$ is also an additional feature in the thermal diffusion term, $(4/3\,\mathrm{Pr}\,R_a)\,\theta''$ although it is not nonlinear. Although the parameter is a denominator, the contribution is still that of thermal conduction heat transfer relative to radiative heat transfer. As R_a increased, thermal conduction becomes progressively larger (for $R_a < 1$ it always dominates thermal radiation) and this causes the flow to declines (fig. 8). For smaller values of R_a thermal radiative heat transfer contributes more and this energizes the nanofluid leading to higher temperatures and a greater thermal boundary layer thickness (fig. 9). It is also noteworthy that the Rosseland model assumes that radiative equilibrium is sustained in the simulations and the

nanofluid is gray and furthermore that the intensity is the black-body intensity at the nanofluid temperature. Implicit in this flux approximation is the requirement that the optical thickness exceeds 3 for reasonable accuracy as noted by Modest (1993) and later Beg et al. (2016). Optical thickness and absorption coefficient are dimensionless quantifications of how much a given medium (nanofluid) retards the passage of thermal radiation. Radiative intensity falls by an exponential factor when optical thickness is unity. Physically optical thickness will be a function of absorption coefficient(k_e) , medium density and propagation distance. Although the flux model is much simpler than other algebraic approximations (e.g. P1 Trauggot model), it does predict fairly accurately the influence of radiative flux.

Figure 11 illustrates the effect of thermophoresis (N_T) on nanofluid temperature distribution. In the phenomenon of thermophoresis, the heated nanoparticles are pushed from a hot surface to a cold area. Thermophoretic body force therefore mobilizes nanoparticle migration from the cylinder surface, and also encourages heat diffusion into the boundary layer away from the wall. This results in an elevation in nanofluid temperature and a concomitant increase in thermal boundary layer thickness. A similar pattern has been reported in many other studies including Prasad et al. (2019) and Raju and Sandeep (2016). The influence of thermophoresis on nanoparticle concentration profiles is illustrated in Fig.12. It is confirmed that thermophoretic body force promotes the transport of nanoparticles away from the heated albeit isothermal cylinder wall into the nanofluid boundary layer regime, and therefore enhances nanoparticle concentration magnitudes. The amplification in magnitudes is also considerably greater than temperatures since thermophoresis is essentially a species diffusion phenomenon which affects thermal field, as simulated in the quadratic temperature derivative term, $N_T(\theta')^2$ in the thermal boundary layer eqn. (11). A simultaneous enhancement in nanoparticle concentration boundary layer thickness is also induced.

The effect of Brownian motion parameter, (N_B) on Williamson nanofluid temperature is exhibited in Fig.13. It is known that larger values of Brownian motion parameter,N_B. (which in the Buongiorno model correspond to smaller nanoparticle sizes and a reduction in ballistic collisions) diminish the nanoparticle concentration i.e. there is a depletion in the volume fraction. In the Buongiorno model, N_B arises in a coupled thermal-species diffusion term, also in the energy eqn. (11), viz $N_B\theta'\phi'$. When this term is magnified, the species diffusion is reduced. A limitation of this model is that actual nanoparticle types e.g. metallic oxides or carbon silicates cannot be simulated since a framework for their properties cannot be accommodated. This is achievable in the Tiwari-Das model, as noted by Beg et al. (2019b). However, the Tiwari-Das model does not feature a mechanism for species diffusion since it omits a concentration balance equation. A possible remedy to this dilemma is the fusion of both models and this is currently under investigation.

Figure 14 exhibits the modification in velocity profiles with Weissenberg rheological number. It is known that Weissenberg number is the ratio between the fluid stress relaxation time and specific process time. This parameter is also a measure of the elastic force in a fluid to the viscous hydrodynamic force. It can also be regarded as the product of shear rate and relaxation time and is generally obtained via scaling the evolution of the stress, based on a careful selection of shear or elongation rate, and the length-scale. Weissenberg number features strongly in the momentum eqn. (10) in the terms, $+2We\xi\left(1-\gamma^{*}\theta\right)f'''\,f''-We\xi\gamma^{*}(f'')^{2}\theta'$. A weak flow deceleration is induced near the cylinder surface whereas further into the boundary layer, transverse to the cylinder, a weak acceleration is observed. The pseudoplastic fluid experiences strong tensile stresses near the wall which prohibit momentum diffusion. These forces are relaxed with greater distance form the wall (cylinder surface) and manifest in a slight enhancement in velocities. This is the dominant effect of greater Weissenberg number which diminishes viscous effects and results in a thinning in the pseudoplastic nanofluid boundary layer thickness. These findings are corroborated with other investigations including Malik et al. (2016). Figure 15 shows the influence of Weissenberg number on temperature profiles. Higher values of Weissenberg number enhance the fluid relaxation time, as a result, momentum diffusion is encouraged. Although We does not feature in the energy eqn. (11), the velocity-temperature coupling terms which include the convective terms, $\xi\left[f'\frac{\partial\theta}{\partial\xi}-\theta'\frac{\partial f}{\partial\xi}\right]$, and $f\theta'$ result in an indirect effect of elasticity on the temperature field. This results in a weak elevation in nanofluid temperature increases with an increase in Weissenberg number and a slight thickening in thermal boundary layer external to the cylinder.

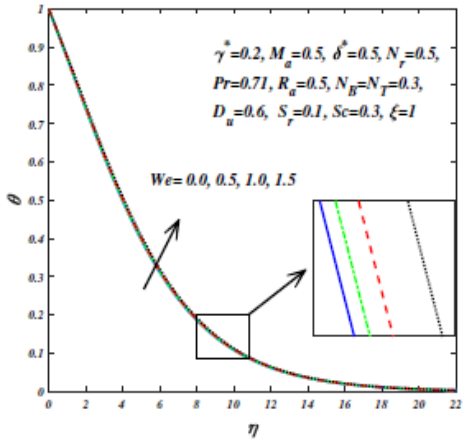

Fig. 15. θ for uplifting values of We.

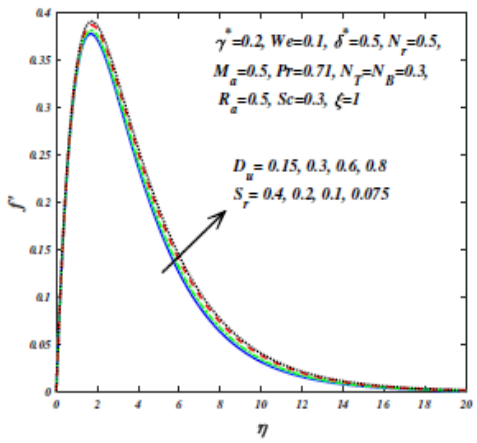

Fig. 16. f' for uplifting & decreasing values of D_u & S_r.

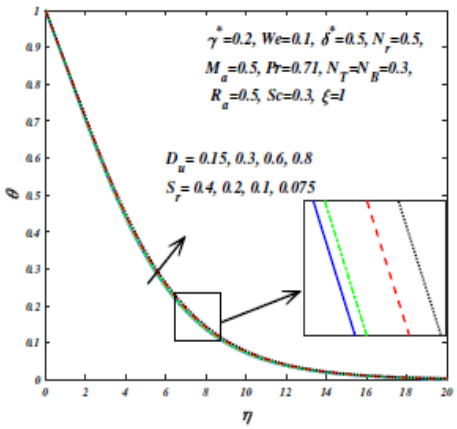

Fig. 17. θ for uplifting& decreasing values of D_u & S_r.

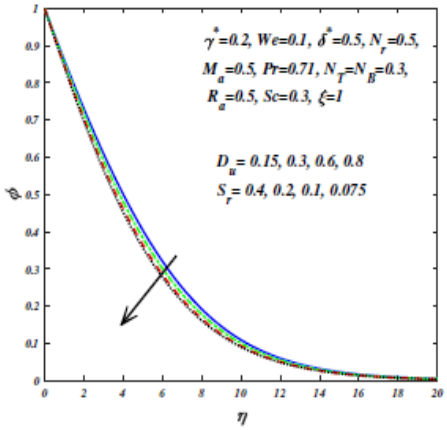

Fig. 18. ϕ for uplifting & decreasing values of D_u & S_r.

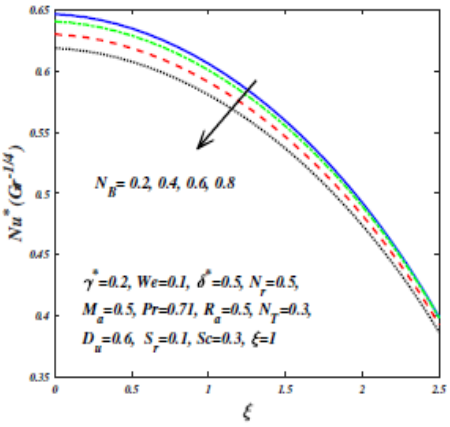

Fig. 19. Nu^* for uplifting values of N_B.

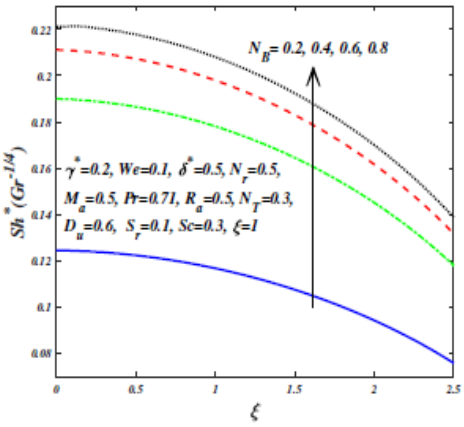

Fig. 20. Sh^* for uplifting values of N_B.

Figures 16-18 are portrayed to display the influence of Soret and Dufour numbers on nanofluid velocity, temperature, and nanoparticle concentration distributions, respectively. Williamson nanofluid velocity and temperature distributions (figs. 16, 17) consistently increase with increment in Dufour number and simultaneous decrement in Soret number. The Dufour diffuso-thermal concentration gradient term, $D_u\phi''$ in the energy eqn. (11) clearly assists in thermal diffusion whereas the Soret thermo-diffusion term, $S_r\theta''$ in the nanoparticle concentration eqn. (12) opposes thermal diffusion. Effectively thermal boundary layer thickness is boosted with greater Du values and depleted with greater Sr values. The modification in velocity is via coupling of the energy and nanoparticle concentration equations to the momentum eqn. (10) in numerous terms, but notably the dual buoyancy (thermo-solutal) term, $+\frac{\mathrm{Sin}\xi}{\xi}(\theta - N_r\phi)$. The contrary behaviour is computed in Fig. 18, wherein

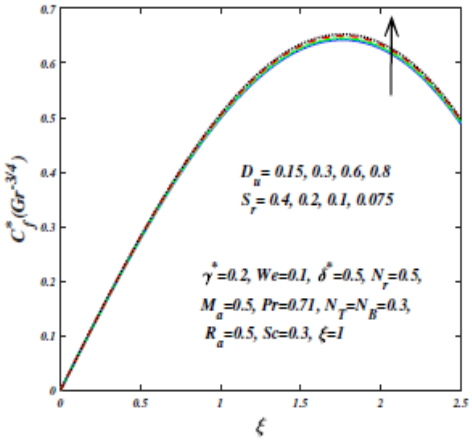

Fig. 21. C_f* for uplifting & decreasing values of D_u & S_r.

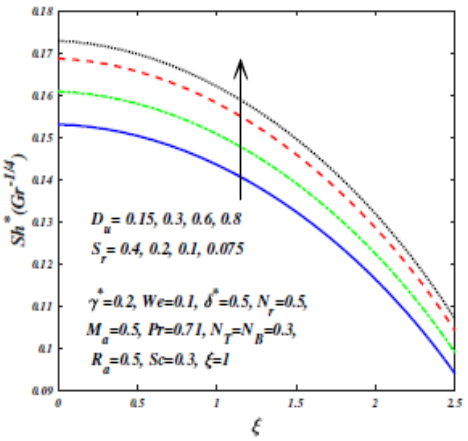

Fig. 22. Sh* for uplifting & decreasing values of D_u & S_r.

an increase in Dufour number and reduction in Soret number is observed to depress nanoparticle concentrations. Stronger Soret effect (thermo-diffusion) is therefore assistive to migration of nanoparticles whereas stronger Dufour effect (diffusothermal) is inhibitive.

Figures 19 and 20 show the impact of Brownian motion parameter on Nusselt and Sherwood numbers at the cylinder surface. A substantial suppression in Nusselt number is induced with increasing values of Brownian motion but the reverse behavior is exhibited (i.e. a strong elevation) in Sherwood numbers. In both plots, the maximum rates of heat and mass transfer at the wall are computed at ξ= 0 (lower stagnation point) and progressively decrease with increasing streamwise coordinate, ξ. Greater Brownian motion clearly encourages heating in the nanofluid (elevation in temperatures, as shown in earlier figures) which draws heat away from the cylinder surface leading to a plummet in Nusselt number. Conversely higher Brownian motion effect (smaller nanoparticles) produces a reduction in nanoparticle concentration values in the nanofluid such that greater translocation of nanoparticles to the boundary (cylinder surface) is mobilized, which explains the considerably magnification in Sherwood number.

Figure 21 illustrates the influence of Soret and Dufour numbers on the skin friction factor i.e. dimensionless shear stress at the cylinder surface. Skin friction factor vanishes at ξ=0, a characteristic of stagnation point flow i.e. the flow is brought to rest here and no shear stress can be generated. With increasing streamwise coordinate, ξ, there is generally a strong monotonic increase in shear stress which is associated with boundary layer growth along the cylinder periphery, as eloquently noted by Glauert and Lighthill (1955) based on an exceptionally rigorous asymptotic analysis. However, there is a terminal point for the elevation in skin friction

which is a result of the eventual decay in momentum along the cylinder surface under fixed species and thermal buoyancy forces. Beyond this critical point, the skin friction begins to descend. Figure 22 displays the influence of Soret and Dufour numbers on the Sherwood number. An increase in Dufour number (and concomitant decrease in Soret number) are observed to markedly increase the rate of mass transfer. A consistently monotonic decay in Sherwood number is computed i.e. the maximum nanoparticle mass transfer to the cylinder surface arises at the stagnation point and progressively diminishes with increasing streamwise coordinate, ξ. This behaviour is clearly only computable with two-dimensional axisymmetric models (ξ, η) which are easily simulated with the Keller-box scheme. The equations (10)-(12) at the stagnation point, $\xi \sim 0$, clearly contract to ordinary differential equations, implying that single-spatial variable models (η) lack the physical rigor for realistic simulations of axisymmetric heat transfer from curved bodies.

Figures 23-25 visualize the impacts of magnetic field, and thermophoresis on the skin-friction factor and heat transfer rate through 3D and contour plots, respectively. It is to be noted that the numerical domain is meshed with 25×25 grid for these visualizations. Figure 23 reveals that skin friction factor is strongly augmented with increasing streamwise coordinate (ξ), again to a critical point (elaborated earlier) at which it peaks ($\xi \sim 2$) thereafter descending steadily with further streamwise distance, as characterized by the parabolic-type topology. Figs. 24 and 25, show that Nusselt number is greatly suppressed with higher M_a and N_T values i.e. heat transfer rate to the wall is a decreasing function of magnetic field and thermophoresis. This corroborates the earlier computations which have shown that temperature is elevated with stronger magnetic field and thermophoretic body force. Since the pseudoplastic nanofluid is heated with both effects, there is an associated decrement in heat transfer to the cylinder surface (boundary) i.e. lower Nusselt numbers. It is noticed from these figures that the lower Lorentz force and lower thermophoresis have a high rate of heat transfer at the stream coordinate ($\xi \sim 1$). Furthermore, increasing values of the Lorentz force and thermophoresis promotes pseudoplastic nanofluid temperature which leads to reduce heat transfer rate.

Figures 26-28 illustrate the streamlines, isothermal and iso-concentration distributions for various values of streamwise coordinate, ξ , magnetic field, M_a and buoyancy ratio parameter, N_r. Fig. 26 shows that the streamlines are denser near the wall (cylinder boundary). It is to be noted that increasing the streamwise coordinate, ξ , from 0.5 to 1.5 serves to intensify the streamlines density whereas a subsequent increment in this coordinate from 1.5 to 2.5, manifests in a relaxation in streamlines. Moreover, higher values of magnetic field and buoyancy ratio parameter (progressively stronger species buoyancy, although for $N_r < 1$ thermal buoyancy is dominant) tend to reduce the density of streamlines, which expand in a fan-like manner the transverse direction (η). Figures 27 and 28 indicate that an increase in

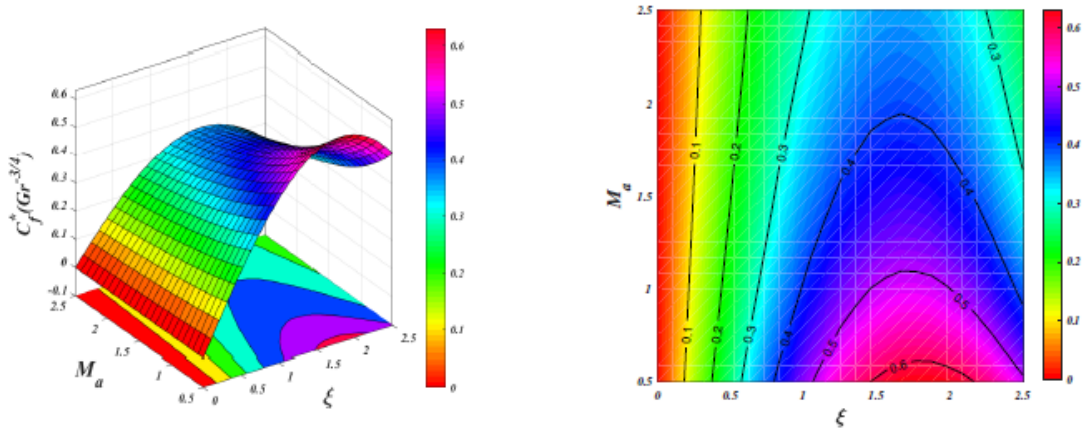

Fig. 23. Impact of M_a on $C_f{}^*$.

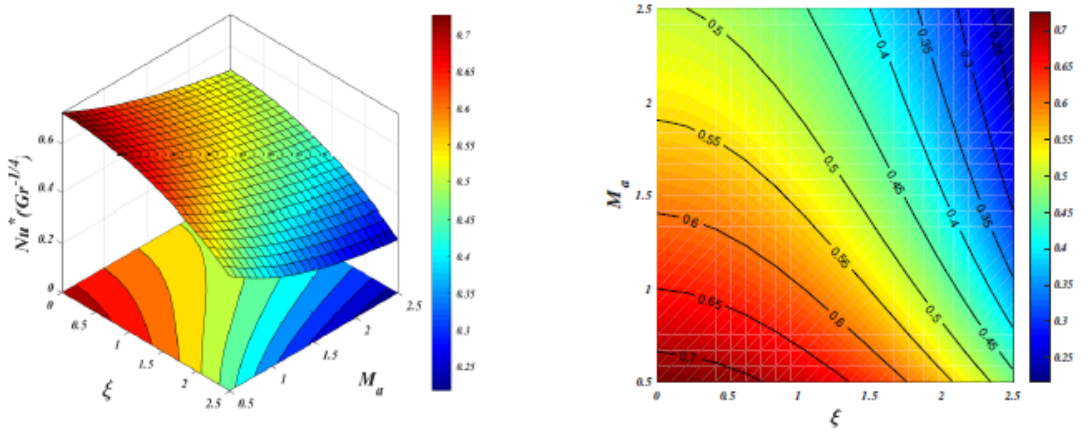

Fig. 24. Impact of M_a on $N_u{}^*$

the streamwise coordinate, ξ, magnetic field and buoyancy ratio parameter, inflate the thermal and mass boundary layer thickness. When strengthening the magnetic field, the Lorentz force triggers electrical conductivity particles in the pseudoplastic nanofluid, causing high heat and concentration in the pseudoplastic nanofluid, thus increasing the heat and mass boundary layer thickness. Generally, N_r expressed as the ratio of thermal buoyancy force of the nanoparticle concentration. N_r only occurs in terms of $\frac{sin\,\xi}{\xi}\,(\theta - N_r\phi)$ in the momentum boundary layer equation. Therefore, nanofluid temperature and nanoparticle concentration are strongly coupled in the nanofluid flow equation. Hence, thermal and mass boundary layer thickness rises slightly by rising values of N_r. Also, higher values of magnetic field and buoyancy ratio parameter generate an enhancement in heat and mass transfer to the wall, as testified to by the lateral fanning in isotherms and iso-concentrations.

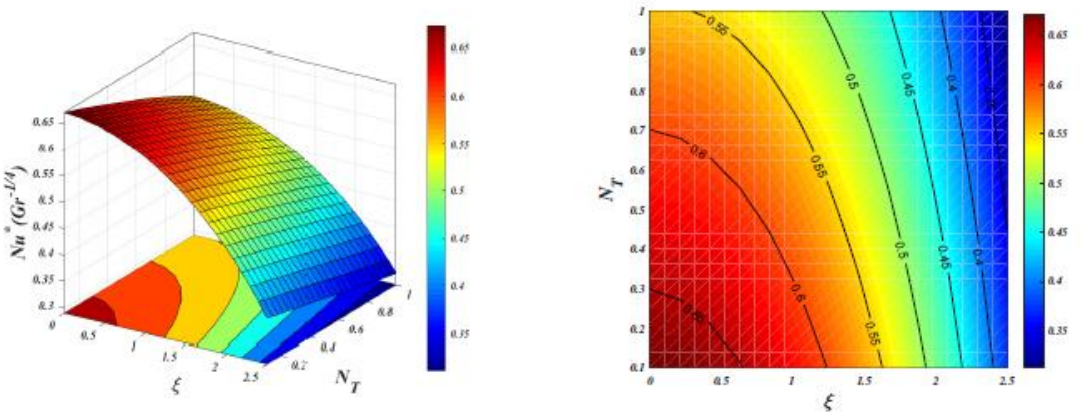

Fig. 25. Impact of N_T on $N_u{}^*$.

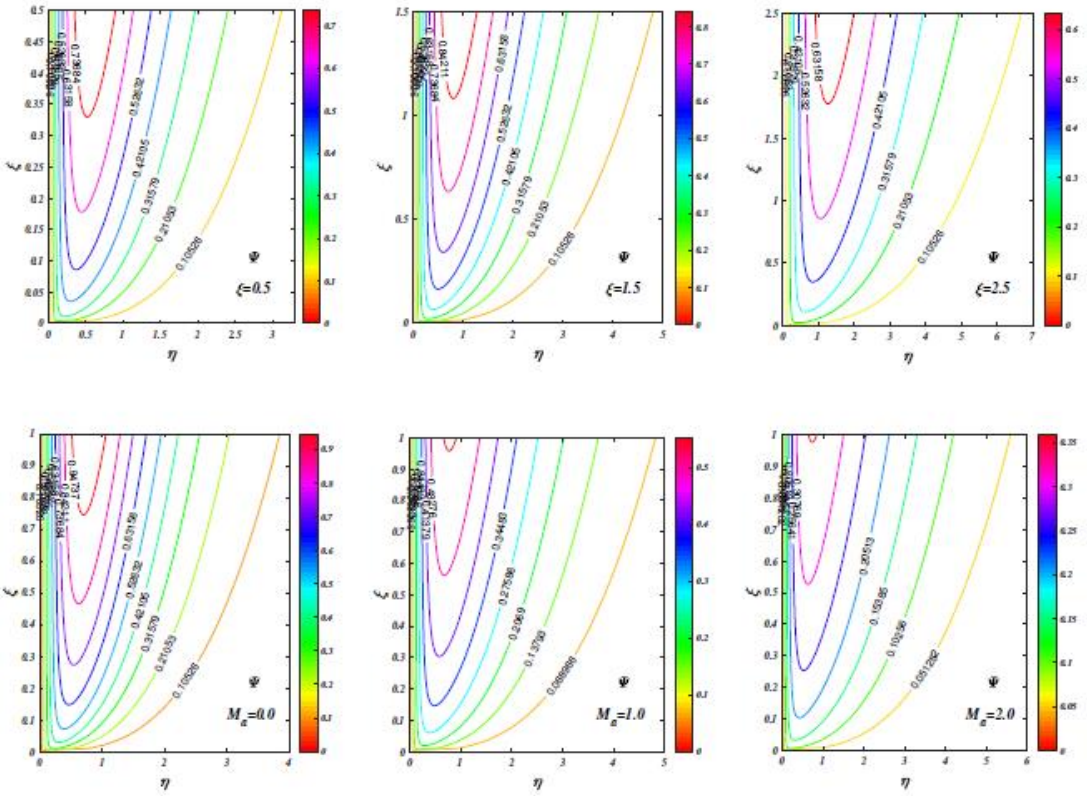

5. Conclusion

Motivated by simulating high-temperature magnetic nano-polymer coating flow transport phenomena, a detailed mathematical study has been presented to investigate the thermosolutal (combined natural convection heat and mass transfer) characteristics in magnetohydrodynamic radiative pseudoplastic nanofluid boundary layer flow external to a circular cylinder under radial static magnetic field,

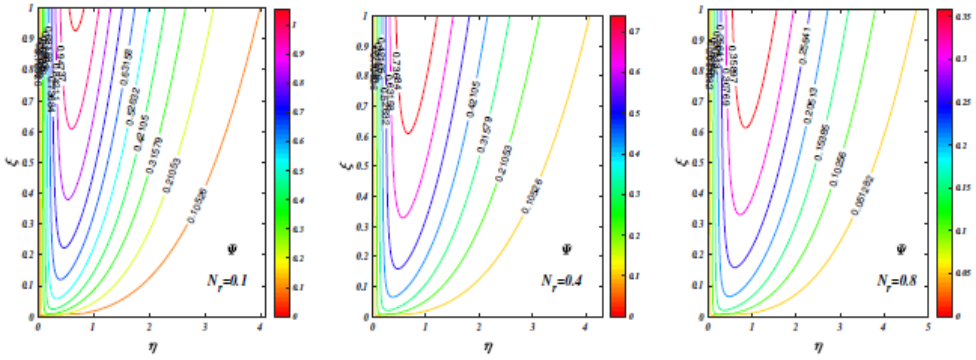

Fig. 26. Streamlines for uplifting values of ξ, M_a and N_r.

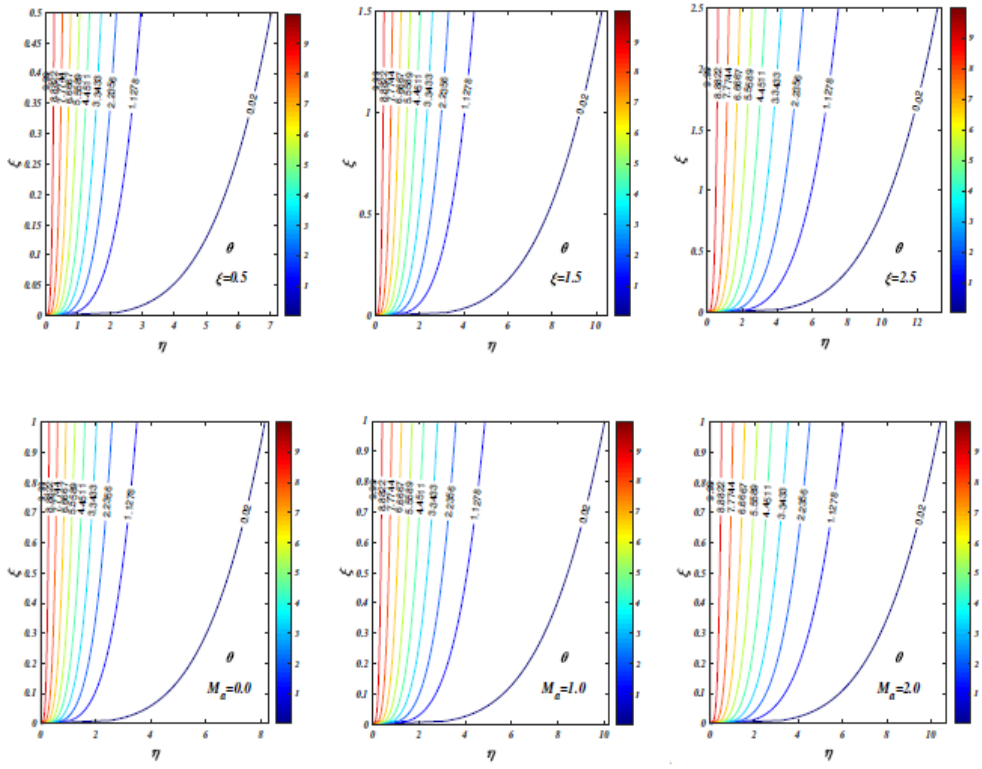

with variable viscosity, variable thermal conductivity, Soret and Dufour effects. The nanoscale transport is modeled by employing the Buongiorno two-component model and the rheological behaviour is accommodated with the Williamson model. Non-similar variables are utilized to transform the dimensional mass, momentum, energy and nanoparticle concentration (volume fraction) equations into dimensionless form. This nonlinear coupled boundary value problem is solved with the implicit finite difference Keller box method under appropriate wall and free stream boundary conditions. Extensive validation of the solutions with earlier published results

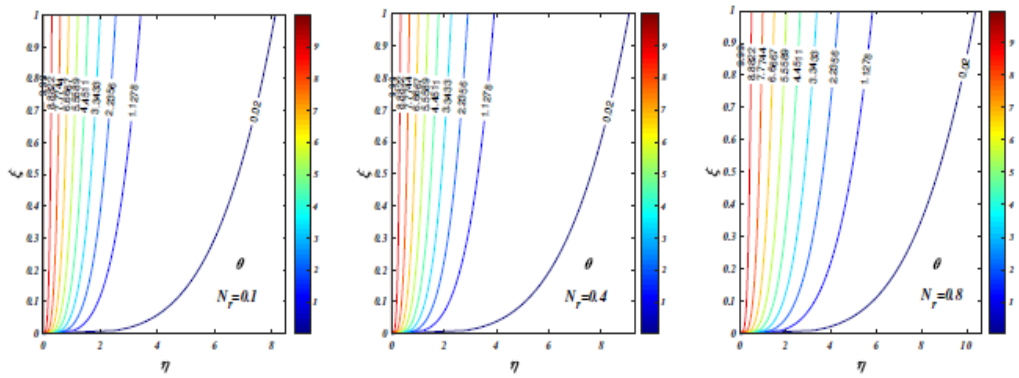

Fig. 27. Isothermal for uplifting values of ξ, M_a and N_r.

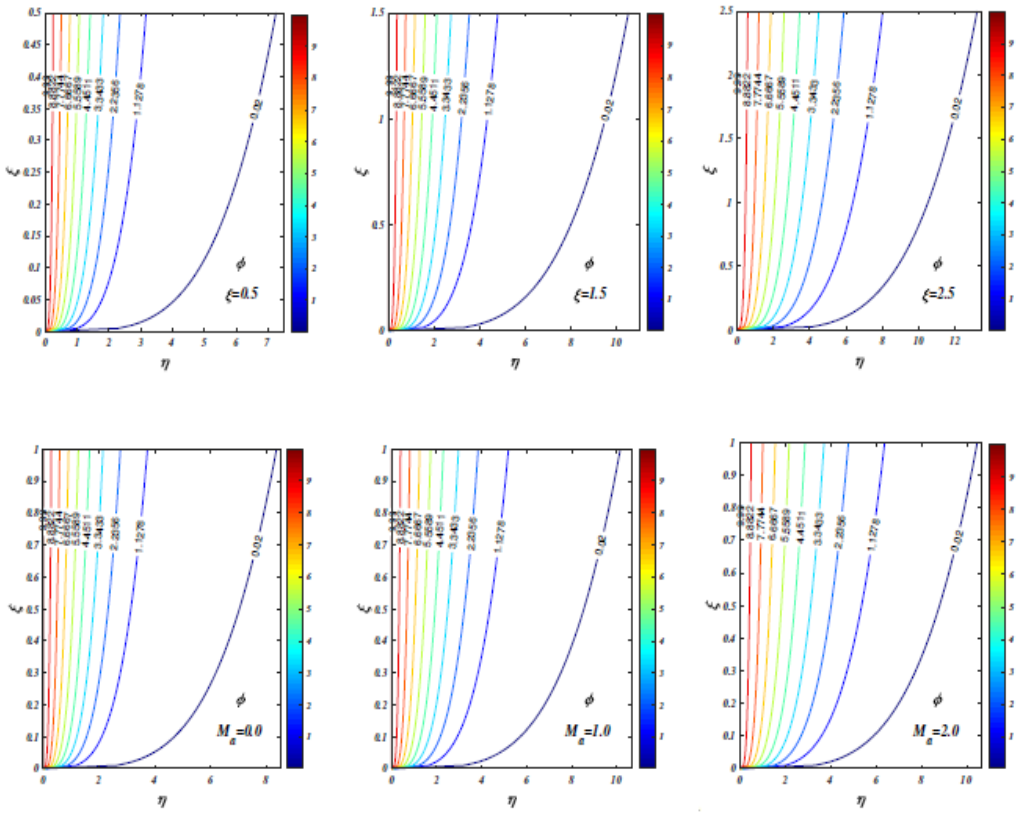

is included. The heat, mass and momentum characteristics are studied for variation in all thermophysical parameters and visualized as graphs versus transverse coordinate, three-dimensional surface plot, contour plots, and streamline, isothermal and iso-concentration plots. Extensive numerical details are provided. The main findings of the current study may be summarized as follows.

- Nanofluid temperature and nanoparticle concentration magnitudes are elevated significantly with increasing magnetic field strength.

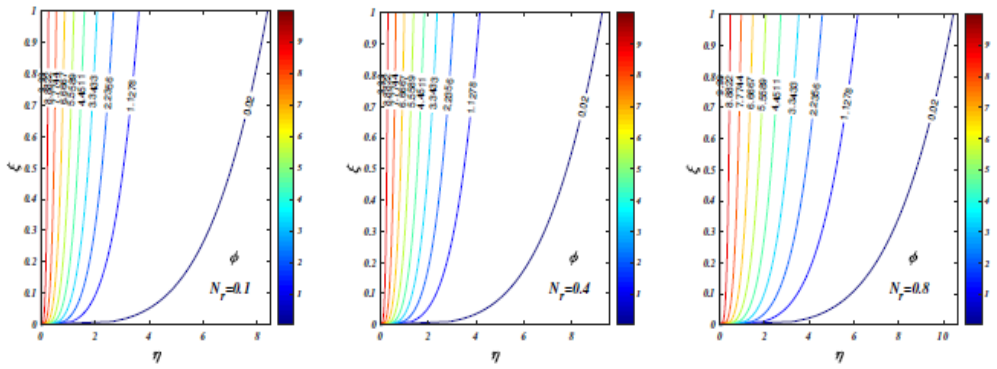

Fig. 28. Isoconcentration for uplifting values of ξ, M_a and N_r.

- Flow deceleration is induced with larger values of the variable viscosity parameter
- Higher values of the thermal conductivity parameter enhance velocity and temperature magnitudes and reduce momentum boundary layer thickness but increase thermal boundary layer thickness.
- An enhancement of Dufour number and simultaneous decrement in Soret number generates marked flow acceleration and heating i.e. greater temperature magnitudes
- An increase in Weissenberg number (i.e. stronger elastic forces relative to viscous forces and greater relaxation time of the pseudoplastic fluid) and thermophoresis parameter increases the nanofluid temperature, although the effect is more pronounced for the latter.
- The density of streamlines is reduced with increasing the magnetic field and buoyancy ratio parameter.
- Increasing magnetic field and buoyancy ratio parameter boost the Nusselt and Sherwood numbers i.e. increase heat and mass transfer to the wall.

The present study has ignored nanoparticle types e.g. metallic oxides. These will be considered using the Tiwari-Das formulation in future investigations. Furthermore, ferromagnetic effects may also be considered including magnetic dipoles which also feature in magnetic nano-materials processing systems.

References

Astanina, M.S., Rashidi, M.M., Sheremet, M.A. and Lorenzini, G. (2019), Effect of porous insertion on convective energy transport in a chamber filled with a temperature-dependent viscosity liquid in the presence of a heat source term, *International Journal of Heat and Mass Transfer* , Vol. 144, pp. 118530.

Animasaun, I.L. (2015), Effects of thermophoresis, variable viscosity and thermal conductivity on free convective heat and mass transfer of non-Darcian MHD dissipative Casson fluid flow with suction and n^{th} order of chemical reaction, *Journal of the Nigerian Mathematical Society*, Vol. 34, pp. 11-31.

Acharya, N., Das, K. and Kundu, P.K. (2019), Influence of multiple slips and chemical reaction on radiative MHD Williamson nanofluid flow in porous medium: A computational framework", *Multidiscipline Modeling in Materials and Structures*, Vol. 15, pp. 630-658.

Anoop K.B., Kabelac, S., Sundararajan, T. and Das, S.K. (2009), Rheological and flow characteristics of nanofluids: Influence of electroviscous effects and particle agglomeration, *Journal of Applied Physics*, Vol.106, pp. 034909.

Basha, H.T., Sivaraj, R., Reddy, A.S. and Chamkha, A. J. (2019), SWCNH/diamond-ethylene glycol nanofluid flow over a wedge, plate and stagnation point with induced magnetic field and nonlinear radiationsolar energy application, *The European Physical Journal Special Topics*, Vol. 228, pp.2531-2551.

Basha, H.T., Sivaraj, R., Reddy, A.S. Chamkha, A.J. and Tilioua M. (2020), Impacts of temperature-dependent viscosity and variable Prandtl number on forced convective FalknerSkan flow of Williamson nanofluid, *SN Applied Sciences*, Vol. 2, pp.477.

Basha, H.T., Sivaraj, R., Prasad, V.R., Beg, O.A. (2020), Entropy generation of tangent hyperbolic nanofluid over a circular cylinder in the presence of nonlinear Boussinesq approximation: a non-similar solution, *Journal of Thermal Analysis and Calorimetry*, DOI: 10.1007/s10973-020-09981-5.

Beg, O.A., Beg, T.A., Bakier, A.Y. and Prasad, V.R. (2009a), Chemically reacting mixed convective heat and mass transfer along inclined and vertical plates with Soret and Dufour effects: Numerical solutions, *International Journal of Applied Mathematics and Mechanics* , Vol. 5, pp. 39-57.

Beg, O.A., Bakier, A.Y. and Prasad, V.R. (2009b), Numerical study of free convection magnetohydrodynamic heat and mass transfer from a stretching surface to a saturated porous medium with Soret and Dufour effects, *Computational Materials Science*, Vol. 46, pp. 57-65.

Beg, O.A., Prasad, V.R., Vasu, B., Reddy, N.B., Li, Q. and Bhargava, R. (2011), Free convection heat and mass transfer from an isothermal sphere to a micropolar regime with Soret/Dufour effects, *International Journal of Heat and Mass Transfer*, Vol. 54, pp. 9-18.

Beg O.A., Ferdows, M., Beg, T.A., Ahmed, T., Wahiduzzaman, M and Alam, M.M. (2016), Radiative optically dense magnetized transient reactive transport phenomena with cross diffusion and dissipation effects: numerical simulations, *Journal of the Taiwan Institute of Chemical Engineers*, Vol.66, pp. 12-26.

Beg, O.A., Espinoza, D.E.S., Kadir, A., Shamshuddin, M. and Sohail, A. (2018), Experimental study of improved rheology and lubricity of drilling fluids enhanced with nanoparticles, *Applied Nanoscience*, Vol. 8, pp. 1069-1090.

Beg, O.A., Beg, T.A., Karim, I., Khan, M.S., Alam, M.M., Ferdows, M. and Shamshuddin M. (2019a), Numerical study of magneto-convective heat and mass transfer from inclined surface with Soret diffusion and heat generation effects: A model for ocean magnetohydrodynamic energy generator fluid dynamics, *Chinese Journal of Physics* , Vol. 60, pp. 167-179.

Beg, O.A., Kuharat, S., Ferdows, M., Das, M., Kadir, A. and Shamshuddin ,M. (2019b). Modeling magnetic nanopolymer flow with induction and nano-particle solid volume fraction effects: solar magnetic nano-polymer fabrication simulation, *Proceedings of the Institution of Mechanical Engineers, Part N: Journal of Nanomaterials, Nanoengineering and Nanosystems* , Vol. 233: pp. 27-45.

Bhatti, M.M., Khalique, C.M., Beg, T., Beg, O.A. and Kadir, A. (2020), Numerical study of slip and radiative effects on magnetic Fe3O4-water-based nanofluid flow from a nonlinear stretching sheet in porous media with Soret and Dufour diffusion, *Modern*

Physics Letters B, Vol. 33, pp.2050026.

Bisht, A. and Sharma, R. (2019), Non-similar solution of Casson nanofluid with variable viscosity and variable thermal conductivity, *International Journal of Numerical Methods for Heat & Fluid Flow*, Vol. 22, pp. 3919-3938.

Cebeci, T. and Bradshaw, P. (1998), Physical and Computational Aspects of Convective Heat Transfer, *Springer*, New York.

Chang, H., Lee, W. S. and Lee, J. (2019), Rheological characteristics of non-Newtonian GPTMS-SiO2 nanofluids, *International Communications in Heat and Mass Transfer*, Vol.106, pp.38-45.

Das, S.K., Choi, S. U. S., Yu ,W. and Pradeep T. (2007), Nanofluids: Science and Technology, *Wiley-Interscience*, New York, USA.

Dhumal, J., Bandgar, S., Zipare, K. and Shahane, G. (2015), Fe_3O_4 ferrofluid nanoparticles: synthesis and rheological behavior, *International Journal of Materials Chemistry and Physics* , Vol. 1, pp. 141-145.

Gaffar, S.A., Prasad, V.R. and Beg, O.A., (2015), Numerical study of flow and heat transfer of non-Newtonian tangent hyperbolic fluid from a sphere with Biot number effects, *Alexandria Engineering Journal* , Vol. 54, pp. 829-841.

Glauert, M.B. and Lighthill, M.J. (1955), The axisymmetric boundary layer on a long thin cylinder, *Proceedings of the Royal Society of London. Series A* , Vol. 224, pp.188.

Hayat, T., Khan, M.I., Farooq, M., Gull, N. and Alsaedi, A. (2016), Unsteady three-dimensional mixed convection flow with variable viscosity and thermal conductivity, *Journal of Molecular Liquids*, Vol. 223, pp. 1297-1310.

Hong, R.Y., Ren, Z.Q., Han, Y.P., Li, H.Z., Zheng, Y. and Ding, J. (2007), Rheological properties of water based Fe_3O_4 ferrofluids, *Chemical Engineering Science*, Vol. 62, pp. 5912-5924.

Hussanan, A., Salleh, M.Z, Khan, I. and Shafie S. (2017), Convection heat transfer in micropolar nanofluids with oxide nanoparticles in water, kerosene and engine oil, *Journal of Molecular Liquids*, Vol. 229, pp. 482-488.

Jaluria, Y. (2013), Thermal issues in materials processing, *Journal of Heat Transfer*, Vol. 135, pp. 061701.

Kafoussias, N.G. and Williams, E.W. (1995), The effect of temperature-dependent viscosity on free-forced convective laminar boundary layer flow past a vertical isothermal flat plate, *Acta Mechanica*, vol. 110, pp. 123-137.

Keller, H.B.(1971), A new difference scheme for parabolic problems. In: numerical solution of partial differential equations II, synspade 1970. *Academic press: Inc.* pp. 327-350.

Kumar, B.R. and Sivaraj, R. (2013), MHD viscoelastic fluid non-Darcy flow over a vertical cone and a flat plate, *International Communications in Heat and Mass Transfer*, Vol.40, pp.1-6.

Kumar, B.R. and Sivaraj, R. (2013), Heat and mass transfer in MHD viscoelastic fluid flow over a vertical cone and flat plate with variable viscosity, *International Journal of Heat and Mass Transfer* ,Vol. 56 , pp.370-379.

Khan, M.I., Nigar M., Hayat T. and Alsaedi A. (2019), On the numerical simulation of stagnation point flow of non-Newtonian fluid (Carreau fluid) with Cattaneo-Christov heat flux, *Computer Methods and Programs in Biomedicine*, Vol. 187, pp.105221.

Latiff, N.A., Uddin, Md. J., Beg, O.A. and Ismail A. I. Md. (2016), Unsteady forced bioconvection slip flow of a micropolar nanofluid from a stretching/ shrinking sheet, *Proceedings of the Institution of Mechanical Engineers, Part N: Journal of Nanomaterials, Nanoengineering and Nanosystems* , Vol. 230 (4) pp. 177-187.

Makinde, O.D. and Olanrewaju, P.O. (2011a), Unsteady mixed convection with Soret and Dufour effects past a porous plate moving through a binary mixture of chemically

reacting fluid, *Chemical Engineering Communications*, Vol. 198, pp. 920-938.

Makinde, O.D., Chinyoka, T. and Rundora, L. (2011b), Unsteady flow of a reactive variable viscosity non-Newtonian fluid through a porous saturated medium with asymmetric convective boundary conditions, *Computers & Mathematics with Applications*, Vol. 62, pp.3343-3352.

Makinde, O.D. and Chinyoka T. (2012), Analysis of unsteady flow of a variable viscosity reactive fluid in a slit with wall suction or injection, *Journal of Petroleum Science and Engineering*, Vol. 94, pp.1-11.

Mansoury, D., Doshmanziari, F.I., Rezaie, S. and Rashidi, M.M. (2019), Effect of Al_2O_3/water nanofluid on performance of parallel flow heat exchangers, *Journal of Thermal Analysis and Calorimetry*, Vol.135, pp.625-643.

Ma, Y., Mohebbi, R., Rashidi, M.M. , Manca, O. and Yang, Z. (2019), Numerical investigation of MHD effects on nanofluid heat transfer, *Journal of Thermal Analysis and Calorimetry*, Vol.135, pp.3197-3213.

Malik, M.Y., Bibi, M., Khan, F. and Salahuddin, T. (2016), Numerical solution of Williamson fluid flow past a stretching cylinder and heat transfer with variable thermal conductivity and heat generation/absorption, *AIP Advances*, Vol.6, pp.035101.

Manjunatha, S. and Gireesha, B.J. (2016), Effects of variable viscosity and thermal conductivity on MHD flow and heat transfer of a dusty fluid, *Ain Shams Engineering* , Vol. 7 , pp.505-515.

Merkin, J.H. (1977), Free convection boundary layers on cylinders of elliptic cross section, *Journal Heat Transfer.*, Vol. 99, pp. 453-457.

Muthtamilselvan, M., Periyadurai, K. and Hee, D. (2018), Impact of nonuniform heated plate on double-diffusive natural convection of micropolar fluid in a square cavity with Soret and Dufour effects, *Advanced Powder Technology*, Vol. 29, pp. 66-77.

Mehmood, R., Tabassum, R., Kuharat,. S., Beg, O.A. and Babie, M. (2019), Thermal slip in oblique radiative nano-polymer gel transport with temperature-dependent viscosity: solar collector nanomaterial coating manufacturing simulation, *Arabian Journal for Science and Engineering*, Vol. 44, 1525-1541.

Modest M. (1992), Radiative Heat Transfer, *MacGraw-Hill*, New York, USA.

Nadeem, S., Ahmad, S. and Muhammad, N. (2017), Cattaneo-Christov flux in the flow of a viscoelastic fluid in the presence of Newtonian heating, *Journal of Molecular Liquids*, Vol. 237, pp.180-184.

Nasrin, R. and Alim, M.A. (2009), MHD free convection flow along a vertical flat plate with thermal conductivity and viscosity depending on temperature, *Journal of Naval Architecture and Marine Engineering*, vol. 6, pp. 72-83.

Norouzi. M., Daghighi, S.Z. and Beg, O.A. (2018), Exact analysis of heat convection of viscoelastic FENE-P fluids through isothermal slits and tubes, *Meccanica*, Vol.53, pp. 817-831.

Pal D., Mandal G. and Vajravalu K., (2016), Soret and Dufour effects on MHD convective radiative heat and mass transfer of nanofluids over a vertical non-linear stretching / shrinking sheet, *Applied Mathematics and Computation* , Vol. 287, pp.184-200.

Prasad, V.R., Gaffar, S.A. and Kumar, B.R. (2019), Non-similar computational solutions for double-diffusive MHD transport phenomena for non-Newtonian nanofluid from a horizontal circular cylinder, *Nonlinear Engineering*, Vol. 485, pp.8470.

Raju, C.S.K. and Sandeep, N. (2016), Heat and mass transfer in MHD non-Newtonian bioconvection flow over a rotating cone/plate with cross diffusion, *Journal of Molecular Liquids*, Vol. 215 , pp. 115-126.

Rashad, A. and Chamkha, A. (2014), Heat and mass transfer by natural convection flow about a truncated cone in porous media with Soret and Dufour effects, *International*

Journal of Numerical Methods for Heat & Fluid Flow, Vol. 24, pp. 595-612.

Reddy, P.S. and Chamkha, A.J. (2016), Soret and Dufour effects on MHD convective flow of Al_2O_3 water and TiO_2 water nanofluids past a stretching sheet in porous media with heat generation / absorption, *Advanced Powder Technology*,Vol.27, pp.1207-1218.

Reddy, G.J., Kumar, M. and Beg, O. A. (2018), Effect of temperature dependent viscosity on entropy generation in transient viscoelastic polymeric fluid flow from an isothermal vertical plate, *Physica A: Statistical Mechanics and its Applications* ,Vol. 510, pp.426-445.

Ruhaila, Md. K., Sivasankaran, S., Bhuvaneswari, M. and Hussein, A.K. (2017), Analytical and numerical study on convection of nanofluid past a moving wedge with Soret and Dufour effects, *International Journal of Numerical Methods for Heat & Fluid Flow*, Vol. 27, pp. 2333-2354.

Sansom, C.L., Jones, P., Dorey, R.A., Beck, C., Stanhope-Bosumpim, A. and Peterson, J. (2013), Synthesis and characterization of $Mn0.5Zn0.5Fe2O4$ and $Fe3O4$ nanoparticle ferrofluids for thermo-electric conversion, *Journal of Magnetism and Magnetic Materials*, Vol. 335 pp. 159-162.

Sivaraj R., Benazir A.J., Srinivas S. and Chamkha A.J. (2019), Investigation of cross-diffusion effects on Casson fluid flow in existence of variable fluid properties, *The European Physical Journal Special Topics* ,Vol. 228, pp.35-53.

Sheikholeslami, M. and Rokni, H.B. (2017), Magnetic nanofluid natural convection in the presence of thermal radiation considering variable viscosity, *The European Physical Journal - Plus* ,Vol. 132, pp. 238.

Sheparovych, R., Sahoo, Y., Motornov, M., Wang, S., Luo, H., Prasad, P.N., Sokolov, I. and Minko, S. (2006), Polyelectrolyte stabilized nanowires from Fe3O4 nanoparticles via magnetic field induced self assembly, *Chemistry of Materials*, Vol. 18, pp. 591-593.

Salahuddin, T., Muhammad, S. and Sakinder, S. (2019), Impact of generalized heat and mass flux models on Darcy-Forchheimer Williamson nanofluid flow with variable viscosity, *Physica Scripta*, Vol. 94, pp. 125201.

Subbarayudu, K., Suneetha, S. and Reddy, P. B. A. (2020), The assessment of time dependent flow of Williamson fluid with radiative blood flow against a wedge, *Propulsion and Power Research*, Vol. 9, pp.87-99.

Vshivkov, S.A. and Rusinova, E. (2017), Effect of magnetic field on the rheological properties of poly (ethylene glycol) and poly (dimethylsiloxane) mixtures with aerosil and iron nanoparticles,*Polymer Science, Series A* , Vol. 59, pp. 764-771.

Williamson, R.V. (1929), The flow of pseudoplastic materials. *Industrial & Engineering Chemistry Research*, Vol. 11, pp. 1108-1111.

Yih, K.A. (2000), Effect of uniform blowing/suction on MHD-natural convection over a horizontal cylinder: UWT or UHF, *Acta Mechanica*, Vol. 144, pp. 17-27.

Appendix A.

To linearize the nonlinear system of equations using Newtons method, we introduce the following iterates:

$$
\begin{aligned}
\omega f_j^{(n)} &= f_j^{(n+1)} - f_j^{(n)}, \\
\omega u_j^{(n)} &= u_j^{(n+1)} - u_j^{(n)}, \\
\omega v_j^{(n)} &= v_j^{(n+1)} - v_j^{(n)}, \\
\omega s_j^{(n)} &= s_j^{(n+1)} - s_j^{(n)}, \\
\omega t_j^{(n)} &= t_j^{(n+1)} - t_j^{(n)}, \\
\omega g_j^{(n)} &= g_j^{(n+1)} - g_j^{(n)}, \\
\omega p_j^{(n)} &= p_j^{(n+1)} - p_j^{(n)}
\end{aligned}
$$

Implementing the above expressions in Eqns. (30)-(36) and neglecting higher-order terms of ω, leads to:

$$
\begin{aligned}
&\omega f_j - \omega f_{j-1} - \frac{h_j}{2}\omega u_j - \frac{h_j}{2}\omega u_{j-1} - (e_1)_j = 0 \\
&\omega u_j - \omega u_{j-1} - \frac{h_j}{2}\omega v_j - \frac{h_j}{2}\omega v_{j-1} - (e_2)_j = 0 \\
&\omega s_j - \omega s_{j-1} - \frac{h_j}{2}\omega t_j - \frac{h_j}{2}\omega t_{j-1} - (e_3)_j = 0 \\
&\omega g_j - \omega g_{j-1} - \frac{h_j}{2}\omega p_j - \frac{h_j}{2}\omega p_{j-1} - (e_4)_j = 0
\end{aligned}
$$

$$
\begin{aligned}
&(a_1)_j\omega v_j + (a_2)_j\omega v_{j-1} + (a_3)_j\omega f_j + (a_4)_j\omega f_{j-1} + (a_5)_j\omega u_j \\
&+(a_6)_j\omega u_{j-1} + (a_7)_j\omega s_j + (a_8)_j\omega s_{j-1} + (a_9)_j\omega t_j \\
&+(a_{10})_j\omega t_{j-1} + (a_{11})_j\omega g_j + (a_{12})_j\omega g_{j-1} - (e_5)_{j-1/2} = 0,
\end{aligned}
$$

$$
\begin{aligned}
&(b_1)_j\omega t_j + (b_2)_j\omega t_{j-1} + (b_3)_j\omega f_j + (b_4)_j\omega f_{j-1} + (b_5)_j\omega u_j + (b_6)_j\omega u_{j-1} \\
&+(b_7)_j\omega s_j + (b_8)_j\omega s_{j-1} + (b_9)_j\omega p_j + (b_{10})_j\omega p_{j-1} - (e_6)_{j-1/2} = 0
\end{aligned}
$$

$$
\begin{aligned}
&(c_1)_j\omega p_j + (c_2)_j\omega p_{j-1} + (c_3)_j\omega f_j + (c_4)_j\omega f_{j-1} + (c_5)_j\omega u_j + (c_6)_j\omega u_{j-1} \\
&+(c_7)_j\omega g_j + (c_8)_j\omega g_{j-1} + (c_9)_j\omega t_j + (c_{10})_j\omega t_{j-1} - (e_7)_{j-1/2} = 0,
\end{aligned}
$$

$$(a_1)_j = 1 - \gamma^* s_{j-1/2} + 2We\xi v_{j-1/2} - 2We\xi\gamma^* v_{j-1/2} s_{j-1/2}$$
$$+h_j \left[-We\xi\gamma^* v_{j-1/2} t_{j-1/2} - \frac{\gamma^*}{2} f_{j-1/2} + \frac{(1+\alpha)}{2} f_{j-1/2} - \frac{\alpha}{2} f_{j-1/2}^{n-1} \right],$$
$$(a_2)_j = -\left(1 - \gamma^* s_{j-1/2} + 2We\xi v_{j-1/2} - 2We\xi\gamma^* v_{j-1/2} s_{j-1/2}\right)$$
$$+h_j \left[-We\xi\gamma^* v_{j-1/2} t_{j-1/2} - \frac{\gamma^*}{2} f_{j-1/2} + \frac{(1+\alpha)}{2} f_{j-1/2} - \frac{\alpha}{2} f_{j-1/2}^{n-1} \right]$$
$$(a_3)_j = h_j \left[\frac{(1+\alpha)}{2} v_{j-1/2} + \frac{\alpha}{2} v_{j-1/2}^{n-1} \right],$$
$$(a_4)_j = (a_3)_j,$$
$$(a_5)_j = h_j \left[-(1+\alpha) u_{j-1/2} - \frac{1}{2}(M) \right],$$
$$(a_6)_j = (a_5)_j,$$
$$(a_7)_j = -\frac{\gamma^*}{2}\left(v_j - v_{j-1}\right) - We\xi\gamma^*\left(v_j - v_{j-1}\right) v_{j-1/2} + \frac{B}{2} h_j,$$
$$(a_8)_j = (a_7)_j,$$
$$(a_9)_j = h_j \left[-\frac{We\xi\gamma^*}{2}\left(v_{j-1/2}\right)^2 - \frac{\gamma^*}{2}\left(v_{j-1/2}\right) \right],$$
$$(a_{10})_j = (a_9)_j,$$
$$(a_{11})_j = -\frac{B}{2} h_j N_r,$$
$$(a_{12})_j = (a_{11})_j,$$

$$(b_1)_j = \frac{1}{\mathrm{Pr}} \left[1 + \frac{4}{3R_a} + \delta^* s_{j-1/2} \right] +$$
$$h_j \left[\frac{\delta^*}{\mathrm{Pr}} t_{j-1/2} + \frac{N_B}{2} p_{j-1/2} + N_T t_{j-1/2} + \frac{(1+\alpha)}{2} f_{j-1/2} - \frac{\alpha}{2} f_{j-1/2}^{n-1} \right],$$
$$(b_2)_j = -\frac{1}{\mathrm{Pr}} \left[1 + \frac{4}{3R_a} + \delta^* s_{j-1/2} \right] +$$
$$h_j \left[\frac{\delta^*}{\mathrm{Pr}} t_{j-1/2} + \frac{N_B}{2} p_{j-1/2} + N_T p_{j-1/2} + \frac{(1+\alpha)}{2} f_{j-1/2} - \frac{\alpha}{2} f_{j-1/2}^{n-1} \right],$$
$$(b_3)_j = h_j \left[\frac{(1+\alpha)}{2} t_{j-1/2} + \frac{\alpha}{2} t_{j-1/2}^{n-1} \right],$$
$$(b_4)_j = (b_3)_j,$$

$$(b_5)_j = h_j\left[-\frac{\alpha}{2}s_{j-1/2} + \frac{\alpha}{2}s^{n-1}_{j-1/2}\right],$$
$$(b_6)_j = (b_5)_j,$$
$$(b_7)_j = \frac{\delta^*}{2\,\mathrm{Pr}}\left(t_j - t_{j-1}\right) + h_j\left[-\frac{\alpha}{2}u_{j-1/2} - \frac{\alpha}{2}u^{n-1}_{j-1/2}\right],$$
$$(b_8)_j = (b_7)_j,$$
$$(b_9)_j = h_j\left[\frac{N_B}{2}t_{j-1/2}\right] + D_u,$$
$$(b_{10})_j = h_j\left[\frac{N_B}{2}t_{j-1/2}\right] - D_u$$
$$(c_1)_j = \frac{1}{Sc} + h_j\left[\frac{(1+\alpha)}{2}f_{j-1/2} - \frac{\alpha}{2}f^{n-1}_{j-1/2}\right],$$
$$(c_2)_j = -\frac{1}{Sc} + h_j\left[\frac{(1+\alpha)}{2}f_{j-1/2} - \frac{\alpha}{2}f^{n-1}_{j-1/2}\right],$$
$$(c_3)_j = h_j\left[\frac{(1+\alpha)}{2}p_{j-1/2} + \frac{\alpha}{2}p^{n-1}_{j-1/2}\right],$$
$$(c_4)_j = (c_3)_j,$$
$$(c_5)_j = h_j\left[-\frac{\alpha}{2}g_{j-1/2} + \frac{\alpha}{2}g^{n-1}_{j-1/2}\right],$$
$$(c_6)_j = (c_5)_j,$$
$$(c_7)_j = h_j\left[-\frac{\alpha}{2}u_{j-1/2} - \frac{\alpha}{2}u^{n-1}_{j-1/2}\right],$$
$$(c_8)_j = (c_7)_j,$$
$$(c_9)_j = \frac{1}{Sc}\frac{N_T}{N_B} + S_r,$$
$$(c_{10})_j = -(c_9)_j,$$

$$(e_5)_{j-1/2} = \left(v_{j-1} - v_j\right)\left[1 - \gamma^* s_{j-1/2} + 2We\xi v_{j-1/2} - 2We\xi\gamma^* v_{j-1/2}s_{j-1/2}\right]$$
$$+We\xi\gamma^* h_j t_{j-1/2}\left(v_{j-1/2}\right)^2 - (1+\alpha)\,h_j f_{j-1/2}v_{j-1/2} + h_j\,(1+\alpha)\,u^2_{j-1/2}$$
$$+\,(M)\,h_j u_{j-1/2} + \gamma^* h_j v_{j-1/2}t_{j-1/2} - \alpha h_j v^{n-1}_{j-1/2}f_{j-1/2} + \alpha h_j f^{n-1}_{j-1/2}v_{j-1/2}$$
$$-Bh_j\left[s_{j-1/2} - N_r\left(g_{j-1/2}\right)\right] + (E_1)^{i-1}_{j-1/2},$$

$$(e_6)_{j-1/2} = \frac{1}{\mathrm{Pr}}\left(t_{j-1} - t_j\right)\left[1 + \frac{4}{3R_a} + \delta^* s_{j-1/2}\right] - \frac{\delta^*}{\mathrm{Pr}}h_j\left(t_{j-1/2}\right)^2$$
$$-N_B h_j t_{j-1/2}p_{j-1/2} - N_T h_j\left(t_{j-1/2}\right)^2 - (1+\alpha)\,h_j f_{j-1/2}t_{j-1/2}$$
$$+h_j\alpha u_{j-1/2}s_{j-1/2} - \alpha h_j s^{n-1}_{j-1/2}u_{j-1/2} + \alpha h_j u^{n-1}_{j-1/2}s_{j-1/2} + \alpha h_j f^{n-1}_{j-1/2}t_{j-1/2},$$
$$-\alpha h_j t^{n-1}_{j-1/2}f_{j-1/2} + D_u\left(p_{j-1} - p_j\right) + (E_2)^{i-1}_{j-1/2},$$

$$(e_7)_{j-1/2} = \frac{1}{Sc}\left(p_{j-1} - p_j\right) - (1+\alpha)\, h_j f_{j-1/2} p_{j-1/2}$$
$$+h_j \alpha u_{j-1/2} g_{j-1/2} - \alpha h_j g^{n-1}_{j-1/2} u_{j-1/2} + \alpha h_j u^{n-1}_{j-1/2} g_{j-1/2} + \alpha h_j f^{n-1}_{j-1/2} p_{j-1/2}$$
$$-\alpha h_j p^{n-1}_{j-1/2} f_{j-1/2} + \left[\frac{1}{Sc}\frac{N_T}{N_B} + S_r\right]\left(t_{j-1} - t_j\right) + (E_3)^{i-1}_{j-1/2}\,.$$

The boundary conditions (29) emerge as:

$$\omega f_0 = 0,\ \omega u_0 = 0,\ \omega s^n_0 = 0,\ \omega g_0 = 0,$$
$$\omega u_J = 0,\ \omega s_J = 0,\ \omega g_J = 0,\ f^n_0 = u^n_0 = 0,$$
$$s^n_0 = 1,\ g^n_0 = 1,\ u^n_J = 0,\ s^n_J = 0,\ g^n_J = 0$$

Step 4:
The block-elimination method is used to compute the linearized difference Eqns. (47)-(56) as outlined by Cebeci and Bradshaw (1984) using the matrix-vector form,

$$A\omega = e$$

where,

$$A = \begin{bmatrix} [A_1] & [C_1] & & & & & \\ [B_2] & [A_2] & [C_2] & & & & \\ & & \ddots & & & & \\ & & & \ddots & & & \\ & & & & \ddots & & \\ & & & & [B_{J-1}] & [A_{J-1}] & [C_{J-1}] \\ & & & & & [B_J] & [C_J] \end{bmatrix},$$

$$\omega = \begin{bmatrix} [\omega_1] \\ [\omega_2] \\ \vdots \\ [\omega_{J-1}] \\ [\omega_J] \end{bmatrix}, \qquad e = \begin{bmatrix} [e_1] \\ [e_2] \\ \vdots \\ [e_{J-1}] \\ [e_J] \end{bmatrix}.$$

The elements of the matrices are as follows:

$$[A_1] = \begin{bmatrix} 0 & 0 & 0 & 1 & 0 & 0 & 0 \\ -\frac{h_j}{2} & 0 & 0 & 0 & -\frac{h_j}{2} & 0 & 0 \\ 0 & -\frac{h_j}{2} & 0 & 0 & 0 & -\frac{h_j}{2} & 0 \\ 0 & 0 & -\frac{h_j}{2} & 0 & 0 & 0 & -\frac{h_j}{2} \\ (a_2)_1 & 0 & (a_{10})_1 & (a_3)_1 & (a_1)_1 & 0 & (a_9)_1 \\ 0 & (b_{10})_1 & (b_2)_1 & (b_3)_1 & 0 & (b_9)_1 & (b_1)_1 \\ 0 & (c_2)_1 & (c_{10})_1 & (c_3)_1 & 0 & (c_1)_1 & (c_9)_1 \end{bmatrix},$$

$$[A_J] = \begin{bmatrix} -\frac{h_j}{2} & 0 & 0 & 1 & 0 & 0 & 0 \\ -1 & 0 & 0 & 0 & -\frac{h_j}{2} & 0 & 0 \\ 0 & -1 & 0 & 0 & 0 & -\frac{h_j}{2} & 0 \\ 0 & 0 & -1 & 0 & 0 & 0 & -\frac{h_j}{2} \\ (a_6)_j & (a_{12})_j & (a_8)_j & (a_3)_j & (a_1)_j & 0 & (a_9)_j \\ (b_6)_j & 0 & (b_8)_j & (b_3)_j & 0 & (b_9)_j & (b_1)_j \\ (c_6)_j & (c_8)_j & 0 & (c_3)_j & 0 & (c_1)_j & (c_9)_j \end{bmatrix}, \quad 2 \le j \le J$$

$$[B_J] = \begin{bmatrix} 0\,0\,0 & -1 & 0 & 0 & 0 \\ 0\,0\,0 & 0 & -\frac{h_j}{2} & 0 & 0 \\ 0\,0\,0 & 0 & 0 & -\frac{h_j}{2} & 0 \\ 0\,0\,0 & 0 & 0 & 0 & -\frac{h_j}{2} \\ 0\,0\,0 & (a_4)_j & (a_2)_j & 0 & (a_{10})_j \\ 0\,0\,0 & (b_4)_j & 0 & (b_{10})_j & (b_2)_j \\ 0\,0\,0 & (c_4)_j & 0 & (c_2)_j & (c_{10})_j \end{bmatrix}, \quad 2 \le j \le J$$

$$[C_J] = \begin{bmatrix} -\frac{h_j}{2} & 0 & 0 & 0\,0\,0\,0 \\ 1 & 0 & 0 & 0\,0\,0\,0 \\ 0 & 1 & 0 & 0\,0\,0\,0 \\ 0 & 0 & 1 & 0\,0\,0\,0 \\ (a_5)_j & (a_{11})_j & (a_7)_j & 0\,0\,0\,0 \\ (b_5)_j & 0 & (b_7)_j & 0\,0\,0\,0 \\ (c_5)_j & (c_7)_j & 0 & 0\,0\,0\,0 \end{bmatrix}, \quad 1 \le j \le J-1$$

$$[\omega_1] = \begin{bmatrix} \omega v_0 \\ \omega p_0 \\ \omega t_0 \\ \omega f_1 \\ \omega v_1 \\ \omega p_1 \\ \omega t_1 \end{bmatrix}, \qquad [\omega_j] = \begin{bmatrix} \omega u_{j-1} \\ \omega g_{j-1} \\ \omega s_{j-1} \\ \omega f_j \\ \omega v_j \\ \omega p_j \\ \delta t_j \end{bmatrix}, \quad 2 \le j \le J$$

$$\text{and } [e_j] = \begin{bmatrix} (e_1)_{j-(1/2)} \\ (e_2)_{j-(1/2)} \\ (e_3)_{j-(1/2)} \\ (e_4)_{j-(1/2)} \\ (e_5)_{j-(1/2)} \\ (e_6)_{j-(1/2)} \\ (e_7)_{j-(1/2)} \end{bmatrix}, \quad 1 \le j \le J$$

Table 3. Impacts of M_a and D_u & S_r on local skin friction coefficient $\left(C_f^*(Gr^{-3/4})\right)$, dimensionless local rate of heat transfer $(Nu^*(Gr^{-1/4}))$ and dimensionless local rate of mass transfer $(Sh^*(Gr^{-1/4}))$ for various values of ξ

Physical Parameters	Values	Physical Quantities	ξ						CPU time(Sec.)
			0	0.5	1	1.5	2	2.5	
M_a	0.0	$C_f^*(Gr^{-3/4})$	0	0.2521	0.4667	0.5634	0.5959	0.4613	8.757743
		$Nu^*(Gr^{-1/4})$	0.6688	0.6499	0.6256	0.5798	0.5282	0.4504	
		$Sh^*(Gr^{-1/4})$	0.1758	0.1710	0.1646	0.1527	0.1391	0.1188	
	0.5	$C_f^*(Gr^{-3/4})$	0	0.2006	0.3612	0.4178	0.4047	0.2421	9.832399
		$Nu^*(Gr^{-1/4})$	0.5839	0.5645	0.5338	0.4802	0.4118	0.3056	
		$Sh^*(Gr^{-1/4})$	0.1542	0.1492	0.1411	0.1272	0.1093	0.0814	
	1.0	$C_f^*(Gr^{-3/4})$	0	0.1681	0.2968	0.3344	0.3061	0.1558	10.132770
		$Nu^*(Gr^{-1/4})$	0.5206	0.5009	0.4666	0.4089	0.3318	0.2136	
		$Sh^*(Gr^{-1/4})$	0.1385	0.1334	0.1245	0.1095	0.0893	0.0581	
	1.5	$C_f^*(Gr^{-3/4})$	0	0.1463	0.2554	0.2837	0.2521	0.1206	9.951370
		$Nu^*(Gr^{-1/4})$	0.4744	0.4549	0.4195	0.3614	0.2835	0.1692	
		$Sh^*(Gr^{-1/4})$	0.1274	0.1223	0.1132	0.0981	0.0778	0.0473	
D_u & S_r	0.15 & 0.4	$C_f^*(Gr^{-3/4})$	0	0.1974	0.3552	0.4109	0.3977	0.2374	8.980526
		$Nu^*(Gr^{-1/4})$	0.5919	0.5722	0.5411	0.4867	0.4172	0.3087	
		$Sh^*(Gr^{-1/4})$	0.1391	0.1347	0.1276	0.1152	0.0992	0.0742	
	0.3 & 0.2	$C_f^*(Gr^{-3/4})$	0	0.1988	0.3577	0.4137	0.4006	0.2393	12.504586
		$Nu^*(Gr^{-1/4})$	0.5913	0.5716	0.5405	0.4860	0.4166	0.3086	
		$Sh^*(Gr^{-1/4})$	0.1465	0.1418	0.1342	0.1210	0.1041	0.0776	
	0.6 & 0.1	$C_f^*(Gr^{-3/4})$	0	0.2006	0.3612	0.4178	0.4047	0.2421	14.960204
		$Nu^*(Gr^{-1/4})$	0.5839	0.5645	0.5338	0.4802	0.4118	0.3056	
		$Sh^*(Gr^{-1/4})$	0.1542	0.1492	0.1411	0.1272	0.1093	0.0814	
	0.8 & 0.075	$C_f^*(Gr^{-3/4})$	0	0.2019	0.3634	0.4204	0.4073	0.2439	9.496180
		$Nu^*(Gr^{-1/4})$	0.5774	0.5582	0.5279	0.4750	0.4075	0.3029	
		$Sh^*(Gr^{-1/4})$	0.1584	0.1532	0.1450	0.1306	0.1122	0.0836	

Table 4. Impacts of N_r and R_a on local skin friction coefficient $\left(C_f^*(Gr^{-3/4})\right)$, dimensionless local rate of heat transfer $(Nu^*(Gr^{-1/4}))$ and dimensionless local rate of mass transfer $(Sh^*(Gr^{-1/4}))$ for various values of ξ

Physical Parameters	Values	Physical Quantities	ξ						CPU time(Sec.)
			0	0.5	1	1.5	2	2.5	
N_r	0.1	$C_f^*(Gr^{-3/4})$	0	0.3210	0.5917	0.6793	0.6852	0.4260	9.280738
		$Nu^*(Gr^{-1/4})$	0.6997	0.6749	0.6419	0.5792	0.5055	0.3873	
		$Sh^*(Gr^{-1/4})$	0.1838	0.1774	0.1688	0.1523	0.1330	0.1020	
	0.3	$C_f^*(Gr^{-3/4})$	0	0.2631	0.4797	0.5531	0.5481	0.3359	9.395184
		$Nu^*(Gr^{-1/4})$	0.6478	0.6256	0.5934	0.5348	0.4631	0.3503	
		$Sh^*(Gr^{-1/4})$	0.1704	0.1647	0.1563	0.1409	0.1222	0.0926	
	0.5	$C_f^*(Gr^{-3/4})$	0	0.2006	0.3612	0.4178	0.4047	0.2421	8.220380
		$Nu^*(Gr^{-1/4})$	0.5839	0.5645	0.5338	0.4802	0.4118	0.3056	
		$Sh^*(Gr^{-1/4})$	0.1542	0.1492	0.1411	0.1272	0.1093	0.0814	
	0.8	$C_f^*(Gr^{-3/4})$	0	0.0941	0.1652	0.1909	0.1746	0.0967	7.504675
		$Nu^*(Gr^{-1/4})$	0.4480	0.4344	0.4093	0.3677	0.3102	0.2203	
		$Sh^*(Gr^{-1/4})$	0.1211	0.1176	0.1112	0.1004	0.0854	0.0614	
R_a	0.1	$C_f^*(Gr^{-3/4})$	0	0.2287	0.4134	0.4791	0.4674	0.2867	12.398441
		$Nu^*(Gr^{-1/4})$	1.4922	1.4514	1.3847	1.2702	1.1242	0.9021	
		$Sh^*(Gr^{-1/4})$	0.2309	0.2229	0.2116	0.1910	0.1657	0.1259	
	0.3	$C_f^*(Gr^{-3/4})$	0	0.2103	0.3791	0.4388	0.4261	0.2570	12.864155
		$Nu^*(Gr^{-1/4})$	0.7667	0.7420	0.7026	0.6341	0.5467	0.4123	
		$Sh^*(Gr^{-1/4})$	0.1828	0.1766	0.1673	0.1507	0.1299	0.0974	
	0.5	$C_f^*(Gr^{-3/4})$	0	0.2006	0.3612	0.4178	0.4047	0.2421	16.059574
		$Nu^*(Gr^{-1/4})$	0.5839	0.5645	0.5338	0.4802	0.4118	0.3056	
		$Sh^*(Gr^{-1/4})$	0.1542	0.1492	0.1411	0.1272	0.1093	0.0814	
	0.8	$C_f^*(Gr^{-3/4})$	0	0.1922	0.3457	0.3998	0.3867	0.2300	14.713669
		$Nu^*(Gr^{-1/4})$	0.4651	0.4496	0.4252	0.3823	0.3276	0.2414	
		$Sh^*(Gr^{-1/4})$	0.1257	0.1220	0.1158	0.1049	0.0907	0.0681	